

Tissue fluidification promotes a cGAS/STING-mediated cytosolic DNA response in invasive breast cancer

Emanuela Frittoli

Fondazione Istituto FIRC di Oncologia Molecolare

Andrea Palamidessi

Fondazione Istituto FIRC di Oncologia Molecolare <https://orcid.org/0000-0002-7134-7023>

Fabio Iannelli

The FIRC Institute of Molecular Oncology, IFOM, Milano

Federica Zanardi

FIRC Institute of Molecular Oncology

Stefano Villa

University of Milan

Leonardo Barzaghi

IFOM <https://orcid.org/0000-0002-3174-6441>

Hind Ando

IFOM

Valeria Cancila

University of Palermo

Galiba Beznuskenko

IFOM

Giulia Della Chiara

IFOM

Massimiliano Pagani

IFOM

Chiara Malinverno

IFOM

Dipanjan Bhattacharya

IFOM

Federica Pisati

IFOM

Weimiao Yu

Institute of Molecular and Cell Biology <https://orcid.org/0000-0001-5092-1009>

Viviana Galimberti

IEO

Giuseppina Bonizzi

IEO

Emanuele Martini

Italian Foundation for Cancer Research <https://orcid.org/0000-0002-3375-7726>

Alexander Mironov

FIRC Institute of Molecular Oncology

ubaldo gioia

IFOM

Fabrizio D'adda di fagagna

IFOM

Chiara Rossi

University of Pavia

Giovanni Bertalot

APPS

Marco Lucioni

University of Pavia

richard tancredi

University of Pavia

paolo Pedrazzoli

University of Pavia

andrea Vecchione

University of Rome, La Sapienza

Cristiuano Perini

IFOM

FRancesco Ferrari

IFOM

Chiara Lanzuolo

ingm

Guilherme Nader

Curie Ist

Marco Foiani

IFOM

Matthieu Piel

Institut Curie <https://orcid.org/0000-0002-2848-177X>

Roberto Cerbino

University of Milan

Fabio Giavazzi

University of Milan <https://orcid.org/0000-0003-4930-0592>

Claudio Tripodo

University of Palermo

Giorgio Scita (✉ giorgio.scita@ifom.eu)

FIRC Institute of Molecular Oncology <https://orcid.org/0000-0001-7984-1889>

Article

Keywords: tissue fluidification, breast cancer, cell density

Posted Date: September 20th, 2021

DOI: <https://doi.org/10.21203/rs.3.rs-845173/v1>

License:   This work is licensed under a Creative Commons Attribution 4.0 International License.

[Read Full License](#)

Tissue fluidification promotes a cGAS/STING-mediated cytosolic DNA response in invasive breast cancer

Emanuela Frittoli^{1,†}, Andrea Palamidessi^{1,†}, Fabio Iannelli¹, Federica Zanardi¹, Stefano Villa², Leonardo Barzaghi¹, Hind Abdo¹, Valeria Cancila³, Galina V. Beznuskenko¹, Giulia della Chiara¹, Massimiliano Pagani^{1,2}, Chiara Malinverno¹, Dipanjan Bhattacharya¹, Federica Pisati¹, Weimiao Yu⁴, Viviana Galimberti⁵, Giuseppina Bonizzi⁵, Emanuele Martini¹, Alexandre Mironov¹, Ubaldo Gioia¹, Fabrizio d'Adda di Fagagna^{1,6}, Chiara Rossi⁷, Marco Lucioni⁷, Richard Tancredi⁸, Paolo Pedrazzoli^{8,9}, Andrea Vecchione¹⁰, Cristiano Petrini¹, Francesco Ferrari^{1,6}, Chiara Lanzuolo¹¹, Guilherme Nader¹², Marco Foiani^{1,13}, Matthieu Piel¹², Roberto Cerbino^{2,¶}, Fabio Giavazzi^{*1,2}, Claudio Tripodo^{*1,3} and Giorgio Scita^{*1,13}

¹IFOM, the FIRC Institute of Molecular Oncology, Via Adamello 16, 20139, Milan, Italy

² Department of Medical Biotechnology and Translational Medicine, University of Milan, 20090 Segrate, Italy

³ Department of Health Sciences, Human Pathology Section, University of Palermo School of Medicine, Via del Vespro 129, 90127, Palermo, Italy

⁴Institute of Molecular and Cell Biology, A*STAR, Singapore, & Bioinformatics Institute, A*STAR, Singapore

⁵European Institute of Oncology (IEO) IRCCS, Via Ripamonti 435, 20141, Milan, Italy

⁶Institute of Molecular Genetics, National Research Council, Pavia, Italy.

⁷ Unit of Anatomic Pathology, Department of Molecular Medicine, Fondazione IRCCS Policlinico San Matteo, University of Pavia, Pavia, Italy

⁸Medical Oncology Unit, Fondazione IRCCS Policlinico San Matteo, Pavia Italy

⁹Department of Internal Medicine and Medical Therapy, University of Pavia, Pavia, Italy

¹⁰Department of Clinical and Molecular Medicine, University of Roma, La Sapienza, Rome, Italy.

¹¹Institute of Biomedical Technologies, National Research Council, Milan, Italy.

¹²Institut Curie and Institut Pierre Gilles de Gennes, PSL Research University, CNRS, UMR-144, Paris, France

¹³ Department of Oncology and Haemato-Oncology, University of Milan, Via Santa Sofia 9/1, 20122, Milan, Italy

Institut Curie and Institut Pierre Gilles de Gennes, PSL Research University, CNRS, UMR-144, Paris, France

¶ Present address: Faculty of Physics of the University of Vienna, Austria.

† These authors contributed equally.

*Corresponding authors- these authors contributed equally to the supervision of the work:

Giorgio.scita@ifom.eu, Fabio.giavazzi@unimi.it, claudio.tripodo@unipa.it.

Lead contact: Giorgio Scita, email:giorgio.scita@ifom.eu

Abstract

The process in which locally confined epithelial malignancies progressively evolve into invasive cancers is often promoted by unjamming, a phase transition from a solid-like to a liquid-like state that occurs in various tissues. Whether this tissue-level mechanical transition impact phenotypes during carcinoma progression remains unclear. We show, here that the large fluctuations in cell density that accompany unjamming result in repeated mechanical deformations of cells and nuclei. Cells react to these protracted mechanical stresses by mounting a mechano-protective response that includes enlarged nuclear size and rigidity, altered heterochromatin distribution, and the remodeling of the perinuclear actin architecture into actin rings. The chronic strains and stresses associated with unjamming together with the reduction of Lamin B1 levels eventually result in DNA damage and nuclear envelope ruptures, with the release of cytosolic DNA that activates a cGAS/STING-dependent cytosolic DNA response gene program. This mechanically-driven transcriptional rewiring ultimately results in a change in cell state, with the emergence of malignant traits, including epithelial-to-mesenchymal plasticity phenotypes and chemo-resistance in invasive breast carcinoma.

One-Sentence Summary: A solid-to-fluid phase transition promotes a pro-inflammatory transcriptional response in invasive breast carcinoma

56
57
58
59
60
61
62
63
64
65
66
67
68
69
70
71
72
73
74
75
76
77
78
79
80
81
82
83
84
85
86
87
88
89
90
91
92
93
94
95
96
97
98
99
100
101
102
103
104
105
106
107
108
109
110
111
112

Introduction and Results

The mechanical and dynamic properties of cells and tissues are emerging as pivotal regulators of cell behavior and fate in physiology and pathology. During carcinogenesis, cancer cells must constantly deal with and adapt to variable mechanical stress, which, in turn, impacts their phenotypes¹. Normal epithelial tissues frequently evolve into solid or jammed masses that are densely packed with cancer cells. To become malignant, a certain degree of fluidity is required for a tissue to be able to proliferate, migrate and disseminate. A recently discovered and less understood process by which cells can acquire migratory behavior is cellular unjamming, a phase transition characterized by collective and cooperative cellular motion akin to fluid flow²⁻⁹. Whether and how unjamming impacts the acquisition of heritable changes that influence tissue state and malignant progression remains unclear.

Ductal adenocarcinoma in situ (DCIS), a precursor of invasive breast cancer, is a remarkable case in point. Firstly, DCISs typically grow at high density within the confinement of the mammary duct lumina, where they may display a highly cohesive growth associated with extreme cell packing and density (*e.g.*, comedonic growth). These conditions expose DCIS to overcrowding and compressive, mechanical stresses that impact their physical state favoring a transition to a solid (jammed) and kinetically-arrested, state. Consistently, nearly 70% of DCIS will not progress, behaving as indolent lesions, which suggests that packing and extreme confinement do exert tumor-suppressive functions. However, 30% of these cancers can overcome the caging imposed by the crowded cellular landscape of packed DCIS, by undergoing a solid (jammed)-to-liquid (unjammed) phase transition, which facilitates the acquisition of cell locomotion and progression to invasive ductal carcinoma (IDC).

We hypothesize that this material-like phase transition is a rapid, short-term adaptive response to mechanical challenging conditions that in addition to promoting collective dissemination of early lesions would also coincidentally result in a long-term, transcriptional-dependent phenotype switch in invasive breast carcinoma.

Endocytic-driven tissue fluidification rewires transcription by promoting a cytosolic DNA response gene signature.

We have recently shown that the expression of the small G protein RAB5A, a pivotal regulator of endosome biogenesis upregulated in human breast cancer and associated with decreased disease-free survival¹⁰, is sufficient to overcome kinetic and proliferation arrest in both normal and tumorigenic epithelia^{2, 8}. RAB5A expression does so by triggering a mechanically-driven phase transition from a solid (or jammed) and immobile state to a flocking fluid hyper-locomotory state that is analogous to animal flocking^{8, 11, 12}. This transition is characterized by the coexistence of long-range, coordinated motion and local liquid-like cell rearrangements^{2, 8, 11-13}. In the context of breast carcinoma, tissue fluidification-via-flocking promotes collective motility and local invasiveness of ductal breast carcinoma². We posit that this mechanically-driven solid-to-fluid transition might also rewire the transcriptional state of early indolent lesion promoting a whole phenotypic switch that impacts tumor progression.

To address this possibility, we began by examining the transcriptional profile of densely packed epithelial monolayers formed by quasi-normal MCF10A cells and the respective oncogenic variant MCF10.DCIS.com cells. Both cell lines were engineered to express RAB5A in a doxycycline-inducible fashion to levels like those found in human invasive breast cancer^{2, 10}. MCF10.DCIS.com cells express oncogenic T24-H-RAS and are used as models for the progression of ductal carcinoma in situ (DCIS) to invasive ductal carcinoma (IDC)^{14, 15}.

As expected, MCF10.DCIS.com cells plated as confluent monolayers are jammed and kinetically arrested^{2, 8}. Induction of RAB5A in both MCF10A and MCF10.DCIS.com jammed monolayers promoted the reawakening of collective motion via flocking^{2, 8}. This was accompanied by robust and highly reproducible alterations in the transcriptional profile (**Fig. 1A and Fig. S1A-C**). Unexpectedly, gene set enrichment analysis revealed the interferon-stimulated gene signature (ISG) as the most significantly enriched in deregulated genes (**Fig. 1C**), albeit interferons (alpha, beta, or gamma) and the corresponding interferon receptor genes were marginally affected (**Fig. S1D**). This suggests that RAB5A-mediated fluidization promotes the rewiring toward an interferon-dependent signature without directly modulating the expression of these cytokines. Noticeably, innate immune responses are also promoted by free endogenous DNA present in the cytosol which is recognized as nonself¹⁶. We thus tested whether RAB5A expression boosted the cytosolic DNA response (CytoDR) program (**Fig. 1C**). Determination of the mRNA levels of the selected most upregulated genes by RT-qPCR or immunoblotting confirmed the effect of RAB5A-fluidification. It further highlighted the massive increase in the expression of a number of these genes, which were induced

113 by more than 100 to 1000 folds with respect to doxycycline control cells (Fig. 1D-E). The upregulation of
114 ISG was also detected in densely packed fluidized MCF10A monolayers by RNA-seq experiments (Fig.
115 S1A-B) and in MCF10.DCIS.com cells grown as tumoroid in low attachment by quantitative PCR of a set
116 of selected genes (Fig. S2A). In all these conditions, we have previously shown that RAB5A promotes a
117 solid-to-liquid transition via flocking and persistent rotational collective motion^{2, 8}. RAB5A expression was
118 sufficient to induce a set of CytoDR genes also in SUM-225, an estrogen, progesterone receptor-negative,
119 and HER2-positive breast carcinoma cell line¹⁷, and in the murine mammary cancer line 4T1¹⁸ (Fig. S2A).

120 Thus, RAB5A induction results in an extended transcriptional rewiring toward a cytosolic gene response
121 state in a variety of fluidized normal and tumorigenic epithelial collectives.

122 The analysis of CytoDR gene expression in single isolated cells revealed that RAB5A only mildly
123 upregulated CytoDR (Fig. S2B), suggesting that RAB5A-mediated transcriptional rewiring is an emergent
124 property of epithelial cell collectives and associated with tissue fluidification. Consistently, the induction of
125 flocking motion via exposure to a hypotonic solution, which promotes tissues fluidification independently
126 from RAB5A expression^{2, 8}, was sufficient to increase CytoDR gene expression in a time-dependent fashion
127 (Fig. S2C and Movie S1). Importantly, the concomitant induction of RAB5A-expression and hypotonic
128 treatment synergically activated flocking fluid motility, as revealed by the increase in typical quantities that
129 exemplify collective motility: the average migration speed v_m , in the velocity correlation length L_C and in the
130 root mean square amplitude of the velocity fluctuations v_{rms} (Fig. S2D and Movie S1). The velocity
131 correlation length L_C is extracted from the spatial correlation function $C_{vv}(r)$ of the vectorial velocity, and
132 quantifies the degree of coordination of the collective cellular motion in terms of the size of a group of cells
133 coherently migrating in the same direction. V_{rms} accounts, instead, for mutual, fluid-like, cell displacements
134 (see Methods for details). The synergic increase in collective motility observed under these conditions also
135 resulted in robust induction of CytoDR gene expression (Fig. S2E). Of note, prolonged hypotonic treatment
136 elicited cellular changes similar to the ones induced upon RAB5A expression, including junctional
137 straightening, increased monolayer rigidity^{2, 8}, and elevation of ERK1/2 activity (Fig. S2F). Endocytic
138 dependent tissue fluidification-via-flocking depends on EGFR activation and internalization into the
139 endosomal compartment which acts as a signaling platform for the activation of ERK1/2 signaling axis^{2, 8}.
140 Treatment with Dynasore to prevent dynamin-dependent internalization or MEK inhibitor to block ERK1/2
141 activation effectively prevented RAB5A-mediated flocking^{2, 8} and impaired CytoDR elevation (Fig. S3A).
142 Finally, neither the induction of RAB5B nor C, which are two highly related members of the RAB5 protein
143 family, promoted unjamming-via-flocking² or elicited CytoDR response (Fig. S3B).

144 We also studied HaCat keratinocyte cells. These cells undergo flocking after induction of RAB5A⁸, which
145 is greatly enhanced following the addition of EGF to quiescent, serum-starved cells¹⁹ (Fig. S3C-E and Movie
146 S2). EGF addition promoted robust flocking, with millimeter-scale correlations in the migration velocities
147 (Fig. S3C-D) but it was insufficient to induce CytoDR genes. CytoDR genes induction required the
148 concomitant expression of RAB5A, which boosted tissue fluidization by greatly enhancing the amplitude of
149 local velocity fluctuations associated with mutual cell displacements (Fig. S3E-F).

150 All in all, these results indicate that endocytic-mediated tissue fluidization occurring via flocking is
151 capable of transcriptionally rewiring cell collectives toward a cytosolic DNA response in a variety of normal
152 and tumorigenic epithelia.

154 Tissue fluidification promotes a cytosolic DNA gene response through the cGAS/STING pathway.

155 Cyclic GMP-AMP synthase (cGAS) is an innate immune sensor of DNA that recognizes cytosolic DNA,
156 resulting in the activation of the signaling adaptor stimulator of interferon genes (STING) and its
157 translocation to the Golgi compartment. At this site, STING activates TANK binding kinase 1 (TBK1) to
158 phosphorylate the transcription factor interferon regulatory factor 3 (IRF3), promoting its nuclear
159 translocation and the expression of type I/III interferon and interferon-stimulated genes²⁰. cGAS recognizes
160 cytosolic DNA derived from invading microbes^{21, 22 23} and also self-DNA from engulfed tumor cells²⁴,
161 damaged mitochondria²⁵⁻²⁷, nuclear DNA damage²⁷⁻³¹.

162 To determine the involvement of the cGAS/STING axis in the activation of CytoDR due to RAB5A-
163 mediated tissue fluidification, we utilized a set of pharmacological and molecular genetic loss-of-function
164 approaches targeting each component of the cGAS/STING/TBK1/IRF3 pathway. Specifically, we silenced
165 cGAS, STING, or IRF3 or treated cells with the cGAS inhibitor, RU.521, the STING antagonist, H-151, or
166 the TBK1/IKK inhibitor, MRT67307, which impairs the phosphorylation of IRF3³². All these treatments
167 robustly hampered the upregulation of CytoDR genes induced by tissue fluidification in MCF10.DCIS.com
168 model tissues (Fig. 2A-B and Fig. S4A). We also targeted key transcription factors acting downstream of
169 the cGAS/STING axis, IRF9, STAT1, and STAT2, which robustly reduced CytoDR gene upregulation (Fig.

170 **2C and Fig. S4A**). Immunoblotting of total cellular lysates of densely packed monolayers revealed that IRF3
171 and both the total and phosphorylated levels of STAT1, but not of cGAS or STING were elevated (**Fig. 2D**),
172 consistent with this pathway being activated by RAB5A-mediated fluidification of MCF10.DCIS.com cell
173 collectives.

174
175 The enzymatic activity of cGAS is activated by double-stranded DNA that leaks or into the
176 cytoplasm from variable sources, including ruptured micronuclei, damaged mitochondria, or fragile and
177 mechanically damaged nuclei. Nuclear damage frequently arises as a consequence of mechanically-
178 induced deformation³³⁻³⁷. We found no evidence of the altered number of micronuclei (**Fig. S4B**). We
179 noticed, instead, that fluidification-via-flocking induced by RAB5A is accompanied by large fluctuation in
180 cell density¹² and cell area (**Fig. 2E-G and Movie S3**), which we hypothesized to be also associated with
181 nuclear deformations. To quantify these deformations, we developed an automated image analysis pipeline
182 to monitor nuclear shape changes over time. We analyzed control and RAB5-expressing MCF10A and
183 MCF10.DCIS.com monolayers. In these cases, tissue fluidification-via-flocking resulted in significantly
184 larger and faster deformations (**Movie S4**), which were quantified by measuring the mean squared nuclear
185 strain $MSS(\tau) \equiv \langle \langle \Delta a_n^2(\tau|t) \rangle_n \rangle_t$ for different delay times τ and extracting the corresponding strain rate $\dot{\gamma}_N \cong$
186 $MSS(\tau)/\tau$ (**Fig. 2H-I**). In previous expressions, $\Delta a_n(\tau|t) \equiv [A_n(t + \tau) - A_n(t)]/A_n(t)$, where $A_n(t)$ is the
187 projected area of the n -th nucleus at time t and the symbols $\langle \cdot \rangle_n$ and $\langle \cdot \rangle_t$ indicate averages performed over
188 all the segmented nuclei and over time, respectively. The increased nuclear strain is the consequence of
189 elevated mechanical stress. Consistently, the mechanosensory and transducer co-transcriptional regulator,
190 YAP1, which is kept off and cytoplasmic-restricted in dense and compact monolayers³⁸, accumulated into
191 nuclei to activate a subset of canonical YAP1 target genes in fluidized cell collectives (**Fig. S4C-E**). We also
192 detected YAP1 reactivation in *ex vivo* organotypic tumour slices from orthotopically-injected
193 MCF10.DCIS.com cells (**Fig. S4F-G**). The induction of RAB5A expression in these cells triggers large
194 collective and invasive motility flow². Thus, endocytic fluidification via flocking imposes large strain and
195 mechanical stress that is directly transferred to cell nuclei.

196 We also noticed that the expression of RAB5A, but not of RAB5B or RAB5C (not shown), in dense
197 monolayers resulted in a significant reduction of the mRNA levels of Lamin B1, but not of Lamin A/C,
198 accompanied by a significant inhibition of the protein levels (**Fig. 2J-K**). Thus, we reasoned that the
199 increased mechanical stress and reduced Lamin B1 levels might compromise nuclear integrity and result
200 in more frequent ruptures of the nuclear envelope (NE). These events might lead to the exposure of DNA
201 to the cytoplasm that, in turn, can trigger cGAS activation. We verified this possibility in multiple and
202 independent ways.

203 Firstly, we expressed cGAS-fused to EGFP (EGFP-cGAS) and monitored its localization and
204 distribution. In dense, kinetically- and proliferation-arrested MCF10.DCIS.com monolayers, EGFP-cGAS
205 displayed a primarily cytoplasmic diffuse staining, as expected^{23, 39}. Laser-mediated ruptures of the NE
206 caused the rapid and focalized accumulation of cGAS at the site of NE damage (**Fig. S5A and Movie S5**).
207 Similar focalized perinuclear restricted localization was seen after RAB5A-induction in flocking fluid
208 monolayers (**Fig. 3A-B**).

209 Secondly, by measuring the amount of cGAMP, the product of cGAS enzymatic activity^{23, 40, 41}, we
210 showed that RAB5A-flocking fluid cells exhibited a significant increase in cGAMP levels (**Fig. 3C**).

211 Thirdly, we monitored in real-time nuclear envelope ruptures through the analysis of the dynamic
212 distribution of the 3NLS-GFP sensor. As shown in **Fig. 3D-E**, while control cells display a nuclear restricted
213 expression of 3NLS-GFP, we detected cytoplasmic distribution of these fluorescent markers in fluidized
214 RAB5A-expressing monolayers, indicative of NE ruptures (**Fig. 3D-E and Movie S6**).

215 Finally, we performed Correlative-Light Electron Microscopy (CLEM) tomography and immune EM to
216 visualize directly the presence of NE ruptures. EGFP-cGAS control and RAB5A-expressing cells were
217 processed for immunofluorescence to detect perinuclear foci of EGFP-cGAS and, subsequently, for EM
218 tomography. Specimens were concomitantly stained with gold-labeled anti-EGFP antibodies to reveal
219 cGAS, which accumulated at sites of condensed chromatin, immediately adjacent to the region where both
220 the inner and outer NE membranes were ruptured (**Fig. 3F and Fig. S5B**). Interestingly, immunofluorescent
221 staining of Lamin A/C also showed that nuclei in RAB5A-fluidized monolayers undergo large deformation
222 and possibly ruptures as indicated by the accumulation of cGAS around distorted nuclei and at the apex of
223 nuclear invagination (**Fig. S5C**).

224
225 **A chronic mechano-response underlies changes in nuclear rigidity, and heterochromatin structure,**
226 **and perinuclear actin polymerization in RAB5A-fluidized collectives**

227 The large fluctuations in tissue density, cell, and nuclear shape suggest that RAB5A-fluidized epithelial
228 collectives are subjected to persistent and chronic mechanical strain and stress. The accumulation of
229 mechanical stress within tissues can compromise tissue integrity^{42, 43}, particularly in cancerous cells, for
230 which mechanical deformations have been shown to induce nuclear rupture and DNA damage^{33, 34, 44}. Both
231 individual cells and epithelial sheets, however, can adapt to acute short-lived stress by mounting a nuclear
232 mechano-protective response that preserves them from widespread genomic damages^{45, 46}. Prolonged
233 stretching or compressive mechanical stresses, however, frequently increases nuclear rigidity and size,
234 elevation in chromatin compaction⁴⁶⁻⁴⁸, and the remodelling of peri-nuclear cytoskeletal actin with the
235 formation of prominent nuclear actin rings^{49, 50}. We hypothesized that endocytic unjamming via flocking in
236 epithelial ensembles exerts protracted mechanical stress, which instigates a protection strategy, which,
237 however, fails eventually resulting in DNA damage. We set out to investigate this possibility.

238 Firstly, we investigated how nuclei respond to motility-induced fluctuation in the local cell density ρ ,
239 which were previously studied in both jammed and fluid monolayers^{12, 51, 52}. To this end, we considered the
240 dependence of the nuclear strain rate $\dot{\gamma}_N = \frac{1}{A} \frac{\partial A}{\partial t}$ on the local monolayer strain rate $\dot{\gamma}_C = -\frac{1}{\rho} \frac{\partial \rho}{\partial t}$, which we
241 estimated as the divergence of the velocity field measured through PIV analysis (Fig. 4A-C). In all cases, a
242 robustly close-to-linear, correlation is found between $\dot{\gamma}_N$ and $\dot{\gamma}_C$, indicating that the nucleus systematically
243 deforms in response to compressive and tensile strains imposed on the cell by the relative motion of its
244 neighbors. The ratio $\dot{\gamma}_C/\dot{\gamma}_N$ between the monolayer and the nuclear strain rate is, thus, an indicator of nuclear
245 stiffness (see Methods for details). RAB5A-fluidized monolayers undergo larger density fluctuations (as
246 captured by the RMS value of the divergence of the velocity field) compared to control-jammed monolayers
247 (Fig. 4B-C). Furthermore, the linear relation between nuclear strain rate and monolayer strain rate is
248 characterized by markedly different slopes in the two cases: in response to the same variation in the cell
249 density, nuclei of RAB5A-fluidized monolayers deform less (by about a factor of 2), showing a markedly
250 stiffer mechanical response compared to controls (Fig 4D-E).

251 Secondly, we showed that nuclear-projected areas are nearly 25% larger in RAB5A-fluidized
252 monolayers as compared to control ones (Fig. S6A-B). Nuclei of RAB5A-expressing cells appeared
253 isotropically and homogeneously enlarged, and their nuclear envelope was under tension. These conditions
254 have recently been shown to mediate the activation of adaptive mechanoresponses increasing the cPLA2-
255 mediated production of arachidonic acid and actomyosin contractility⁵³⁻⁵⁵. Noticeably, treatment with MK-
256 886 inhibits 5-lipoxygenase-activating protein (FLAP) and COX-1, thereby blocking the conversion of
257 arachidonic acid into prostaglandins⁵⁶ or with Blebbistatin, which impairs actomyosin contractility, partially
258 reduced the RAB5A-dependent tissue fluidification-mediated upregulation of cytoDR (Fig. S6C).

259 Thirdly, to probe the heterochromatin state, we initially examined the nuclear levels of H3K27me3.
260 RAB5A-fluidized DCIS cells display a small but significant increase in H3K27m3-heterochromatin marks
261 (Fig. 4F-G), which were prominently enriched at the nuclear periphery (Fig. 4F-I). Analysis of the top 100
262 upregulated genes revealed among the top transcription factors, EZH2, a histone H3 Lysine 27 N-
263 methyltransferase, and SUZ12, which is a key component of the Polycomb Repressor complex -2 (PRC2)
264 (Fig. S6D). These enzymes deposit H3K27m3 to repress transcription and promote chromatin compaction
265 in response to nuclear mechanical stress⁵⁷. Additionally, a pre-ranked gene set enrichment analysis showed
266 enrichment in genes that can be targeted by PRC2 (Fig. S6E). Consistently, silencing of EZH2 or SUZ12
267 abrogated the increase in H3K27me3-heterochromatin marks (Fig. 4G-H and Fig. S6F-G). Polycom-
268 mediated heterochromatin compaction contributes to nuclear rigidity and nuclear resistance to deformation.
269 It may also generate anchoring points for the LINC (Linker of Nucleoskeleton and Cytoskeleton) complex
270 to strengthen the interaction between the cytoskeleton and the nucleus, thus making it easier for the
271 cytoskeleton to move the nucleus within the cell^{58, 59}. Consistently, measurement of the mean square
272 angular displacement $MSAD(\tau)$ revealed that nuclei in RAB5A-fluidized MCF10A or MCF10.DCIS.com
273 monolayers displayed faster rotational dynamics, both in terms of the angular velocity ω associated with
274 the observed short-time ballistic scaling $MSAD(\tau) \sim (\omega\tau)^2$ and of the rotational diffusion coefficient D_R
275 capturing the long-time diffusive-like behavior $MSAD(\tau) \sim 2D_R\tau$ (Fig. S7A). Additionally, while nuclei of
276 control epithelial monolayers display a significant instantaneous correlation between nuclear orientation
277 and direction of motion, there is an evident loss of correlation in RAB5A-fluidized cells, and specifically in
278 MCF10.DCIS.com cells (Fig. S7B). Thus, RAB5A-fluidized collectives, display faster and more persistent
279 rotational dynamics: all features that might contribute to exert increased nuclear mechanical strain.

280 The chronic mechanical stress together with Lamin B1 reduction in RAB5A-fluidized monolayers might
281 also elicit genome-wide structural alterations in constitutive H3K9me3 normally associated with the lamina,
282 as a mechanism to dissipate forces⁴⁹. We employed Sammy-Seq and H3K9me3 CHIP-seq to verify this

283 possibility. Sammy-Seq is a high-throughput sequencing-based method for genome-wide characterization
284 of chromatin accessibility, which can detect architectural rearrangements of lamina-associated
285 heterochromatin domains (LADs)⁶⁰. RAB5-fluidized monolayers displayed no changes in the H3K9me3-
286 genome-wide ChIP-seq profile (Fig. S7C), but a consistent reduction in the SAMMY-seq signal for
287 heterochromatin regions (Fig. S7D).

288 Next, we found that tissue fluidification is also accompanied by the perinuclear remodelling of the actin
289 cytoskeleton. Inspection of cell and cytoskeletal architecture revealed drastic and time-dependent
290 alterations in their organization in fluidized monolayers. Firstly, doxycycline induction of RAB5A resulted in
291 perturbations of the shape of cells that switched from regular polygons in jammed monolayers to irregular
292 and variably elongated shapes in fluidized collectives (Fig. 4J and Fig. S7E). This result agrees with the
293 concept that cell shape elongation and variance in cell shape are strictly associated with unjamming and
294 tissue fluidification^{61, 62}. This change of shape was accompanied by the presence of supracellular actin
295 structures, by the increase in cytoplasmic polymerized actin, and by the formation of prominent perinuclear
296 actin rings (Fig. 4J-K and Fig. S7E). As expected, interference with actin polymerization by the addition of
297 latrunculin B to sequester monomeric actin, inhibited the formation of these structures. More surprisingly,
298 also CytoDR gene upregulation was found to be inhibited (Fig. S7F-G).

299 RAB5A-fluidized monolayers mount a complex mechano-protective response, which leads to decrease
300 nuclear pliability and softness, suggesting the possibility that these monolayers are less capable of
301 dissipating mechanical energy to prevent DNA damage⁴⁹. Consistently, RAB5A-flocking monolayers
302 display elevated DNA damage, as evidenced by the significant increase in 53BP1 and γ H2AX foci (Fig. 5A-
303 C), and in the tail moment determined by neutral DNA comet assays^{63, 64} (Fig. 5F-G).

304 **RAB5A-expression triggers cGAS activation and DNA damage in invasive ductal carcinoma *in vivo*** 305 **and human patients**

306 Next, we studied whether the observed nuclear mechano-perturbations leading to cGAS activation, and
307 increase in DNA damage observed *in vitro* are also relevant in pathological tissues. We first turned to
308 orthotopic xenograft murine models of DCIS. Control and RAB5A-MCF10.DCIS.com cells were injected
309 into the mammary fat pads of immunocompromised animals. In this system, RAB5A induction increased
310 CytoDR, as expected (Fig. S8A). The immunohistochemical analysis further revealed that RAB5A tumors
311 had elevated γ H2AX positive cells (Fig. 6A-B), and enhanced levels of cGAS, which display a perinuclear
312 dotted or crescent-like appearance (Fig. 6C-D). This pattern is similar to the one seen in human DCIS (see
313 Fig. S9C-D to compare the distribution of cGAS in human DCIS with local infiltrative areas), likely reflecting
314 its activation by cytoplasmic DNA. The specificity of anti-cGAS antibodies was verified using FFPE
315 MCF10.DCIS.com cells knocked down for cGAS (Fig. S8B-C).

316 Next, we focused on a set of human ductal carcinoma *in situ* with different degrees of local invasiveness.
317 RAB5A expression was frequently elevated displaying a graded increase in expression at the margin of
318 locally invasive foci of DCIS (Fig. 6E-G and S9A). In these regions, we have just shown that nuclei are
319 significantly less rounded and display an increased number of cells expressing γ H2AX as compared to the
320 bulk of the tumor⁶⁵. Multiplex Opal fluorescent staining revealed that marginal cells, which had elevated
321 RAB5A, also displayed increased γ H2AX, and phosphorylated checkpoint kinase 1 (pChk1) (Fig. 6E-G and
322 S9A), a marker of persistent DNA damage⁶⁶, and more relevantly of cGAS (Fig. 6G-H and S9B). The latter
323 protein was significantly more elevated in cells expressing high levels of RAB5A at the invasive foci of
324 human DCIS, where it displayed either a perinuclear dotted or crescent-like appearance, similar to the one
325 detected in RAB5A-expressing MCF10.DCIS.com orthotopic xenografts (Fig. S9C-D). Similar graded
326 expression of RAB5A associated with elevated γ H2AX and cGAS was also detected in patient-derived
327 breast cancer organoids (Fig. S9E).

328 Quantitative analysis of a set of living breast cancer organoids labeled with NuLight to monitor nuclear
329 motion revealed that some of them displayed persistent rotational motion and all the key features of a
330 flocking fluid (Movie S7). By combining 3D image registration with a differential analysis of the residual
331 intensity fluctuations (see Methods and Ref.⁶⁷ for details), we decoupled the rigid body contribution
332 associated with the global rotation of the organoid from the internal rearrangement dynamics, which is
333 captured by the overlap parameter $Q(\tau)$. Persistently rotating organoids (characterized by an average
334 angular speed larger than 0.03 *cycles/h*, roughly corresponding to one full rotation per day) also displayed
335 markedly faster internal dynamics, with a relaxation time τ^* at least two times shorter than the static ones
336 (Fig. S10A-C and Movie S8). This latter discovery further supports the pathophysiological relevance of
337 fluidification via flocking. Next, we subjected the two static and the three rotating organoids to a genomic
338 analysis by RNA-seq. Despite the limited number of samples, we found that rotating fluid organoids display
339

340 a significantly elevated expression of RAB5A (Fig. S10D), enrichment in several genes belonging to the
341 interferon-alpha stimulated and Interferon related DNA damage resistance signature (Fig. S10E-H).
342 Whereas the analysis of the top deregulated genes pointed to PRC2 complex components, SUZ12 and
343 EZH2, as a key altered transcription factor in rotating organoids (Fig. S10I).
344

345 **Tissue fluidification via flocking enriches for plastic epithelial-to-mesenchymal traits and increases** 346 **chemoresistance**

347 Chronic stimulation of cGAS-STING signaling has been shown to exert either immunoprotective or pro-
348 tumorigenic effects. For example, by establishing an immune-suppressive tumor microenvironment, cGAS
349 activation can promote a transition toward a mesenchymal state⁶⁸ and resistance to chemotherapeutic
350 agents that result in increased metastasis⁶⁹. In addition, an experimentally derived interferon-related DNA
351 damage resistance signature (IRDS) highly related to CytoDR has been associated with resistance to
352 chemotherapy and/or radiation across different cancer cell lines⁷⁰. Hence, we hypothesize that endocytic-
353 mediated tissue fluidification might promote the acquisition of chemoresistance and plastic EMT traits.

354 Firstly, we noticed that several mesenchymal markers, including CDH2, ZEB1, MMP13, EGF, and
355 AXIN2, were reproducibly and significantly upregulated in RAB5A-expressing fluidized-via-flocking
356 MCF10.DCIS.com (Fig. 7A). Several canonical mesenchymal factors, including the master EMT regulators,
357 SNAIL1 and 2 and TWIST, were unaffected (not shown), suggesting the acquisition of what has been
358 defined as plastic EMT transcriptional state (EMP)⁷¹. This was corroborated by the morphological analysis,
359 which indicated that RAB5A induction leads to the loss of the typical cuboidal epithelial shape with the
360 acquisition of an elongated mesenchymal morphology (Fig. 7B). Notably, the expression of this set of genes
361 was dependent on the activity of YAP1/TAZ (Fig. S11A-B), consistent with the concept that the EMP
362 phenotype switch is, at least in part, a mechanoresponsive process⁷²⁻⁷⁷.

363 Finally, we determined whether the elevation of CytoDR is associated with the acquisition of
364 chemoresistance to anti-tumorigenic drugs. Firstly, by examining the differential gene expression profile of
365 control and fluidized monolayers, we observed a concordant interferon-related DNA damage resistance
366 signature that has been previously associated with resistance to chemotherapy and/or radiation particularly
367 in breast cancer⁷⁰ (Fig. S7C). Additionally, we found that RAB5A -expressing cells were slightly more
368 resistant to the topoisomerase inhibitor, etoposide, and remarkably more resistant to docetaxel (Fig. 7D-
369 E). In this latter case, while most control cells display a grossly defective nuclear morphology in keeping
370 with the antimitotic activity of taxols, more than 60 % of RAB5A-expressing displayed intact and unperturbed
371 nuclei (Fig. 7F).
372

373 **Conclusions and outlook**

374
375 The tissue-level phase transition from a solid or jammed to a liquid-like or unjammed state has been recently
376 proposed to be a complementary or, possibly, alternative gateway to cell invasion in both normal epithelia
377 during development³ and in solid carcinoma during malignant progression^{2, 4, 9, 61}. Experimental evidence
378 indicated that the progression from an indolent, quasi benign ductal breast carcinoma lesion to invasive
379 ductal carcinoma is associated with the acquisition of a flocking-fluid mode of collective motion induced by
380 the upregulation of the endocytic, promigratory gene, RAB5A^{2, 10}. Indeed, fluidized RAB5A-expressing
381 DCIS spheroids display a radial gradient of fluidity with cells at the periphery in contact with the ECM
382 exhibiting faster dynamics and increased tissue fluidization². These rapid and dynamic changes impose
383 mechanical strains and stresses on the surrounding ECM fibers, ultimately resulting in their remodeling and
384 the generation of tracks and channels that facilitate collective invasion².

385 Here, we showed that in addition to these short-time features, the altered mechanics of fluidized tissues
386 is also accompanied by a robust, cell-autonomous, and long-lived transcriptional rewiring mediated by the
387 cGAS/STING-dependent, proinflammatory response.

388 Previous studies showed that cancer cell invasion into the confinement of narrow channels and gaps of
389 interstitial tissues exerts large mechanical strains on the nucleus that, when above a certain threshold, can
390 lead to nuclear envelope ruptures (NER) and transient leakage of DNA into the cytosol^{33, 34, 44, 78}. These
391 events, however, are typically short-lived as NER are efficiently and rapidly repaired by the Endosomal
392 Sorting Complex Required for Transport (ESCORT III) system^{33, 79} and the Barrier-to-autointegration factor
393 (BAF)⁸⁰, and have not been shown to promote permanent cell fate changes or transcriptional rewiring. BAF,
394 specifically, can also inhibit cGAS binding to DNA and cGAS activation⁸¹. Tissue fluidification via flocking
395 results, however, in a persistent and a long-lived, chronic mechanical stress state. Tumor cells react to
396 these challenges by mounting a set of diverse mechanoprotective response strategies⁴⁹, including

397 increasing nuclear stiffening, alterations in the distribution and structures of heterochromatin, loss of Lamin
398 B1, and the formation of persistent and nuclear protective actin rings⁴⁹. However, as mechanical strains
399 driven by large-scale tissue fluctuations and small-scale nuclear deformations persist in fluidized tissues,
400 nuclear mechanoprotection eventually fails. This results in frequent and repeated NER, and in
401 mechanically-induced, aberrantly elevated DNA damage. These combined events might lead to the
402 accumulation of fragmented DNA that overcome the inhibitory action of BAF and potently activates
403 sustained cGAS/STING signaling, leading to rewiring of the transcriptional profile of DCIS toward an innate
404 immunity, interferon-like, inflammatory response. Remarkably, such changes are a cell-intrinsic and an
405 emerging property of tumor cell collectives, rather than dependent on the interaction of the malignant tissue
406 with the microenvironment. It must be noted, however, that mechanical perturbations associated with tissue
407 fluidification via unjamming have recently been shown to be driven also by extreme ECM-mediated
408 confinement during invasive growth of triple-negative mammary cancer⁸² or by compressive stresses⁸³.
409 These microenvironmental-driven alterations might also contribute to the activation of proinflammatory,
410 transcriptional changes. Indeed, we showed that in naturally occurring DCIS the activation of cGAS and the
411 increased elevation of γ H2AX frequently accompany the formation of infiltrative foci that mark the transition
412 toward a more invasive phenotype. At these sites, like in model DCIS in 2D and 3D, and in living breast
413 cancer organoids, invasive buds display a graded elevation of RAB5A expression, associated with
414 persistent angular motility and local gradients of fluidification. These local alterations in tissue dynamics are
415 expected to increase chronic mechanical stress, thereby instigating conditions that facilitate NER and
416 cGAS/STING elevation. Recently, we have also shown that extreme confinement in DCIS cancer model
417 cells might be sufficient to promote NERs⁶⁵. These events, however, are relatively transient, but sufficient
418 to promote the nuclear entry of exonucleases, such as TREX1. TREX1 nuclear re-localization, in turn,
419 critically contributes to damage the DNA, under conditions in which the leakage of DNA into the cytoplasm
420 is limited and cGAS is not activated⁶⁵.

421 Recently, skin epidermis stem/progenitor cells subjected to relatively short cycles of stretching have
422 been shown to trigger amplitude-dependent supracellular and nuclear mechanoresponses⁴⁹. These include
423 the formation of transient actin rings and a nuclear tension-mediated, Ca^{++} dependent reduction in the levels
424 of H3K9me3 heterochromatin, resulting in chromatin fluidification and nuclear softening to dissipate
425 mechanical energy⁴⁹. Sustained chromatin fluidification, in turn, led to transcriptional repression and
426 decreased expression of cell identity and differentiation genes⁴⁹. Unjamming via flocking imposes, however,
427 qualitative and quantitative different mechanical strains, that, nevertheless, elicit a robust set of
428 mechanoprotective responses. These protective strategies, like in skin epidermis stem/progenitor cells,
429 include the permanent formation of actin rings, but no alterations in the global constitutive levels of
430 H3K9me3 heterochromatin, which is, nevertheless, architecturally reorganized. In addition, we detected a
431 slight global increase and a robust redistribution at the nuclear periphery of the facultative H3K27me3
432 marks. Notably, this latter modification has been shown to occur upon long-term (6-24 hours) stretching,
433 and to be responsible for increase nuclear rigidity^{46, 49}, similar to what we found in fluidized normal and
434 oncogenic mammary epithelia. Persistency of these alterations in the presence of constant mechanical
435 stress exerted on cells and nuclei results in NER, leakage of cytoplasmic DNA, and DNA damage. Thus,
436 cells mount distinctive mechanoprotective responses that are not only dependent on the time and extent of
437 mechanical perturbations but are likely cell context related.

438 In the oncogenic DCIS setting, this mechanism of long-term adaptation to perturbed mechanics leads
439 to the potent activation of the cGAS/STING axis. It is of note, that recently this cytosolic DNA response axis
440 has been shown to induce a pro-tumorigenic phenotype, characterized by a shift toward a mesenchymal
441 state and increased chemoresistance^{68, 84}, as we also found in our system. It is however likely that in an
442 immune-proficient context, the same axis might trigger a pro-immunogenic, potentially anti-tumoral
443 response. Whether this is the case is certainly a matter of future investigation. Similarly, it will be paramount
444 to determine what are the factors or conditions that tune the mechanically-driven cGAS/STING activation
445 toward either a pro-tumorigenic or pro-immunogenic fate.
446

References

1. Northey, J.J., Przybyla, L. & Weaver, V.M. Tissue Force Programs Cell Fate and Tumor Aggression. *Cancer Discov* **7**, 1224-1237 (2017).
2. Palamidessi, A. *et al.* Unjamming overcomes kinetic and proliferation arrest in terminally differentiated cells and promotes collective motility of carcinoma. *Nat Mater* **18**, 1252-1263 (2019).
3. Mongera, A. *et al.* A fluid-to-solid jamming transition underlies vertebrate body axis elongation. *Nature* **561**, 401-405 (2018).
4. Oswald, L., Grosser, S., Smith, D.M. & Kas, J.A. Jamming transitions in cancer. *J Phys D Appl Phys* **50**, 483001 (2017).
5. Bi, D., Yang, X., Marchetti, M.C. & Manning, M.L. Motility-Driven Glass and Jamming Transitions in Biological Tissues. *Physical Review X* **6**, 021011 (2016).
6. Park, J.A. *et al.* Unjamming and cell shape in the asthmatic airway epithelium. *Nat Mater* **14**, 1040-1048 (2015).
7. Sadati, M., Taheri Qazvini, N., Krishnan, R., Park, C.Y. & Fredberg, J.J. Collective migration, and cell jamming. *Differentiation* **86**, 121-125 (2013).
8. Malinverno, C. *et al.* Endocytic reawakening of motility in jammed epithelia. *Nat Mater* **16**, 587-596 (2017).
9. Park, J.A., Atia, L., Mitchel, J.A., Fredberg, J.J. & Butler, J.P. Collective migration and cell jamming in asthma, cancer, and development. *J Cell Sci* **129**, 3375-3383 (2016).
10. Frittoli, E. *et al.* A RAB5/RAB4 recycling circuitry induces a proteolytic invasive program and promotes tumor dissemination. *J Cell Biol* **206**, 307-328 (2014).
11. Giavazzi, F. *et al.* Flocking transitions in confluent tissues. *Soft Matter* **14**, 3471-3477 (2018).
12. Giavazzi, F. *et al.* Giant fluctuations and structural effects in a flocking epithelium. *Journal of Physics D: Applied Physics* **50**, 384003 (2017).
13. Cerbino, R. *et al.* Disentangling collective motion and local rearrangements in 2D and 3D cell assemblies. *Soft Matter* (2020).
14. Miller, F.R., Santner, S.J., Tait, L. & Dawson, P.J. MCF10DCIS.com xenograft model of human comedo ductal carcinoma in situ. *J Natl Cancer Inst* **92**, 1185-1186 (2000).
15. Hu, M. *et al.* Regulation of in situ to invasive breast carcinoma transition. *Cancer cell* **13**, 394-406 (2008).
16. Hu, M.M. & Shu, H.B. Innate Immune Response to Cytoplasmic DNA: Mechanisms and Diseases. *Annu Rev Immunol* **38**, 79-98 (2020).
17. Kaur, H. *et al.* RNA-Seq of human breast ductal carcinoma in situ models reveals aldehyde dehydrogenase isoform 5A1 as a novel potential target. *PLoS ONE* **7**, e50249 (2012).
18. Pulaski, B.A. & Ostrand-Rosenberg, S. Mouse 4T1 breast tumor model. *Curr Protoc Immunol* **Chapter 20**, Unit 20 22 (2001).
19. Lang, E. *et al.* Coordinated collective migration and asymmetric cell division in confluent human keratinocytes without wounding. *Nat Commun* **9**, 3665 (2018).
20. Chen, Q., Sun, L. & Chen, Z.J. Regulation and function of the cGAS-STING pathway of cytosolic DNA sensing. *Nat Immunol* **17**, 1142-1149 (2016).
21. Gao, D. *et al.* Cyclic GMP-AMP synthase is an innate immune sensor of HIV and other retroviruses. *Science* **341**, 903-906 (2013).
22. Lahaye, X. *et al.* The capsids of HIV-1 and HIV-2 determine immune detection of the viral cDNA by the innate sensor cGAS in dendritic cells. *Immunity* **39**, 1132-1142 (2013).
23. Sun, L., Wu, J., Du, F., Chen, X. & Chen, Z.J. Cyclic GMP-AMP synthase is a cytosolic DNA sensor that activates the type I interferon pathway. *Science* **339**, 786-791 (2013).
24. Woo, S.R. *et al.* STING-dependent cytosolic DNA sensing mediates innate immune recognition of immunogenic tumors. *Immunity* **41**, 830-842 (2014).
25. Rongvaux, A. *et al.* Apoptotic caspases prevent the induction of type I interferons by mitochondrial DNA. *Cell* **159**, 1563-1577 (2014).
26. White, M.J. *et al.* Apoptotic caspases suppress mtDNA-induced STING-mediated type I IFN production. *Cell* **159**, 1549-1562 (2014).
27. West, A.P. *et al.* Mitochondrial DNA stress primes the antiviral innate immune response. *Nature* **520**, 553-557 (2015).
28. Gluck, S. *et al.* Innate immune sensing of cytosolic chromatin fragments through cGAS promotes senescence. *Nat Cell Biol* **19**, 1061-1070 (2017).

- 504 29. Harding, S.M. *et al.* Mitotic progression following DNA damage enables pattern recognition within
505 micronuclei. *Nature* **548**, 466-470 (2017).
- 506 30. Mackenzie, K.J. *et al.* cGAS surveillance of micronuclei links genome instability to innate immunity.
507 *Nature* **548**, 461-465 (2017).
- 508 31. Yang, Z., Maciejowski, J. & de Lange, T. Nuclear Envelope Rupture Is Enhanced by Loss of p53
509 or Rb. *Mol Cancer Res* **15**, 1579-1586 (2017).
- 510 32. Clark, K. *et al.* Novel cross-talk within the IKK family controls innate immunity. *Biochem J* **434**, 93-
511 104 (2011).
- 512 33. Raab, M. *et al.* ESCRT III repairs nuclear envelope ruptures during cell migration to limit DNA
513 damage and cell death. *Science* **352**, 359-362 (2016).
- 514 34. Denais, C.M. *et al.* Nuclear envelope rupture and repair during cancer cell migration. *Science* **352**,
515 353-358 (2016).
- 516 35. Ahmed, B. *et al.* Mitochondrial and Chromosomal Damage Induced by Oxidative Stress in Zn(2+)
517 Ions, ZnO-Bulk and ZnO-NPs treated Allium cepa roots. *Sci Rep* **7**, 40685 (2017).
- 518 36. Nagayama, K. & Fukuei, T. Cyclic stretch-induced mechanical stress to the cell nucleus inhibits
519 ultraviolet radiation-induced DNA damage. *Biomech Model Mechanobiol* **19**, 493-504 (2020).
- 520 37. Shah, P., Wolf, K. & Lammerding, J. Bursting the Bubble - Nuclear Envelope Rupture as a Path to
521 Genomic Instability? *Trends Cell Biol* **27**, 546-555 (2017).
- 522 38. Dupont, S. *et al.* Role of YAP/TAZ in mechanotransduction. *Nature* **474**, 179-183 (2011).
- 523 39. Wang, H. *et al.* cGAS is essential for the antitumor effect of immune checkpoint blockade. *Proc*
524 *Natl Acad Sci U S A* **114**, 1637-1642 (2017).
- 525 40. Gao, P. *et al.* Cyclic [G(2',5')pA(3',5')p] is the metazoan second messenger produced by DNA-
526 activated cyclic GMP-AMP synthase. *Cell* **153**, 1094-1107 (2013).
- 527 41. Gentili, M. *et al.* The N-Terminal Domain of cGAS Determines Preferential Association with
528 Centromeric DNA and Innate Immune Activation in the Nucleus. *Cell Rep* **26**, 2377-2393 e2313
529 (2019).
- 530 42. Casares, L. *et al.* Hydraulic fracture during epithelial stretching. *Nat Mater* **14**, 343-351 (2015).
- 531 43. Harris, A.R. *et al.* Characterizing the mechanics of cultured cell monolayers. *Proc Natl Acad Sci U*
532 *S A* **109**, 16449-16454 (2012).
- 533 44. Xia, Y. *et al.* Nuclear rupture at sites of high curvature compromises retention of DNA repair factors.
534 *J Cell Biol* **217**, 3796-3808 (2018).
- 535 45. Latorre, M. & Humphrey, J.D. Modeling mechano-driven and immuno-mediated aortic
536 maladaptation in hypertension. *Biomech Model Mechanobiol* **17**, 1497-1511 (2018).
- 537 46. Le, H.Q. *et al.* Mechanical regulation of transcription controls Polycomb-mediated gene silencing
538 during lineage commitment. *Nat Cell Biol* **18**, 864-875 (2016).
- 539 47. Damodaran, K. *et al.* Compressive force induces reversible chromatin condensation and cell
540 geometry-dependent transcriptional response. *Mol Biol Cell* **29**, 3039-3051 (2018).
- 541 48. Bonnevie, E.D. *et al.* Cell morphology and mechanosensing can be decoupled in fibrous
542 microenvironments and identified using artificial neural networks. *Sci Rep* **11**, 5950 (2021).
- 543 49. Nava, M.M. *et al.* Heterochromatin-Driven Nuclear Softening Protects the Genome against
544 Mechanical Stress-Induced Damage. *Cell* **181**, 800-817 e822 (2020).
- 545 50. Shao, X., Li, Q., Mogilner, A., Bershadsky, A.D. & Shivashankar, G.V. Mechanical stimulation
546 induces formin-dependent assembly of a perinuclear actin rim. *Proc Natl Acad Sci U S A* **112**,
547 E2595-2601 (2015).
- 548 51. Zehnder, S.M. *et al.* Multicellular density fluctuations in epithelial monolayers. *Phys Rev E Stat*
549 *Nonlin Soft Matter Phys* **92**, 032729 (2015).
- 550 52. Zehnder, S.M., Suaris, M., Bellaire, M.M. & Angelini, T.E. Cell Volume Fluctuations in MDCK
551 Monolayers. *Biophys J* **108**, 247-250 (2015).
- 552 53. Venturini, V. *et al.* The nucleus measures shape changes for cellular proprioception to control
553 dynamic cell behavior. *Science* **370** (2020).
- 554 54. Lomakin, A.J. *et al.* The nucleus acts as a ruler tailoring cell responses to spatial constraints.
555 *Science* **370** (2020).
- 556 55. Enyedi, B., Jelcic, M. & Niethammer, P. The Cell Nucleus Serves as a Mechanotransducer of
557 Tissue Damage-Induced Inflammation. *Cell* **165**, 1160-1170 (2016).
- 558 56. Koeberle, A. *et al.* MK-886, an inhibitor of the 5-lipoxygenase-activating protein, inhibits
559 cyclooxygenase-1 activity and suppresses platelet aggregation. *Eur J Pharmacol* **608**, 84-90
560 (2009).

- 561 57. Heo, S.J. *et al.* Differentiation alters stem cell nuclear architecture, mechanics, and mechano-
562 sensitivity. *Elife* **5** (2016).
- 563 58. Liu, L. *et al.* Chromatin organization regulated by EZH2-mediated H3K27me3 is required for OPN-
564 induced migration of bone marrow-derived mesenchymal stem cells. *Int J Biochem Cell Biol* **96**,
565 29-39 (2018).
- 566 59. Gerlitz, G. & Bustin, M. The role of chromatin structure in cell migration. *Trends Cell Biol* **21**, 6-11
567 (2011).
- 568 60. Sebestyén, E. *et al.* SAMMY-seq reveals early alteration of heterochromatin and deregulation of
569 bivalent genes in Hutchinson-Gilford Progeria Syndrome. *Nat Commun* **11**, 6274 (2020).
- 570 61. Grosser, S. *et al.* Cell and Nucleus Shape as an Indicator of Tissue Fluidity in Carcinoma. *Physical*
571 *Review X* **11**, 011033 (2021).
- 572 62. Atia, L. *et al.* Geometric constraints during epithelial jamming. *Nat Phys* **14**, 613-620 (2018).
- 573 63. Wojewodzka, M., Buraczewska, I. & Kruszewski, M. A modified neutral comet assay: elimination of
574 lysis at high temperature and validation of the assay with anti-single-stranded DNA antibody. *Mutat*
575 *Res* **518**, 9-20 (2002).
- 576 64. Van Kooij, R.J. *et al.* The neutral comet assay detects double-strand DNA damage in selected and
577 unselected human spermatozoa of normospermic donors. *Int J Androl* **27**, 140-146 (2004).
- 578 65. Nader, G.P.F. *et al.* Compromised nuclear envelope integrity drives tumor cell invasion. *bioRxiv*,
579 2020.2005.2022.110122 (2020).
- 580 66. Niziolek-Kierecka, M., Dreij, K., Lundstedt, S. & Stenius, U. gammaH2AX, pChk1, and Wip1 as
581 potential markers of persistent DNA damage derived from dibenzo[a,l]pyrene and PAH-containing
582 extracts from contaminated soils. *Chem Res Toxicol* **25**, 862-872 (2012).
- 583 67. Cerbino, R. *et al.* Disentangling collective motion and local rearrangements in 2D and 3D cell
584 assemblies. *Soft Matter* **17**, 3550-3559 (2021).
- 585 68. Bakhoun, S.F. *et al.* Chromosomal instability drives metastasis through a cytosolic DNA response.
586 *Nature* **553**, 467-472 (2018).
- 587 69. Coussens, L.M. & Werb, Z. Inflammation and cancer. *Nature* **420**, 860-867 (2002).
- 588 70. Weichselbaum, R.R. *et al.* An interferon-related gene signature for DNA damage resistance is a
589 predictive marker for chemotherapy and radiation for breast cancer. *Proc Natl Acad Sci U S A* **105**,
590 18490-18495 (2008).
- 591 71. Yang, J. *et al.* Guidelines and definitions for research on epithelial-mesenchymal transition. *Nat*
592 *Rev Mol Cell Biol* **21**, 341-352 (2020).
- 593 72. Wei, S.C. *et al.* Matrix stiffness drives epithelial-mesenchymal transition and tumour metastasis
594 through a TWIST1-G3BP2 mechanotransduction pathway. *Nat Cell Biol* **17**, 678-688 (2015).
- 595 73. Kim, H.Y., Jackson, T.R. & Davidson, L.A. On the role of mechanics in driving mesenchymal-to-
596 epithelial transitions. *Semin Cell Dev Biol* **67**, 113-122 (2017).
- 597 74. Scott, L.E., Weinberg, S.H. & Lemmon, C.A. Mechanochemical Signaling of the Extracellular Matrix
598 in Epithelial-Mesenchymal Transition. *Front Cell Dev Biol* **7**, 135 (2019).
- 599 75. Yuan, Y. *et al.* YAP overexpression promote the epithelial-mesenchymal transition and
600 chemoresistance in pancreatic cancer cells. *Mol Med Rep* **13**, 237-242 (2016).
- 601 76. Shao, D.D. *et al.* KRAS and YAP1 converge to regulate EMT and tumor survival. *Cell* **158**, 171-
602 184 (2014).
- 603 77. Zhang, J. *et al.* YAP-dependent induction of amphiregulin identifies a non-cell-autonomous
604 component of the Hippo pathway. *Nat Cell Biol* **11**, 1444-1450 (2009).
- 605 78. Pfeifer, C.R. *et al.* Constricted migration increases DNA damage and independently represses cell
606 cycle. *Mol Biol Cell* **29**, 1948-1962 (2018).
- 607 79. Radulovic, M. & Stenmark, H. ESCRTs in membrane sealing. *Biochem Soc Trans* **46**, 773-778
608 (2018).
- 609 80. Halfmann, C.T. *et al.* Repair of nuclear ruptures requires barrier-to-autointegration factor. *J Cell*
610 *Biol* **218**, 2136-2149 (2019).
- 611 81. Guey, B. *et al.* BAF restrict cGAS on nuclear DNA to prevent innate immune activation. *Science*
612 **369**, 823-828 (2020).
- 613 82. Ilina, O. *et al.* Cell-cell adhesion and 3D matrix confinement determine jamming transitions in breast
614 cancer invasion. *Nat Cell Biol* **22**, 1103-1115 (2020).
- 615 83. Kilic, A. *et al.* Mechanical forces induce an asthma gene signature in healthy airway epithelial cells.
616 *Sci Rep* **10**, 966 (2020).

- 617 84. Vashi, N. & Bakhom, S.F. The Evolution of STING Signaling and Its Involvement in Cancer.
618 *Trends Biochem Sci* (2021).
619

620 **Acknowledgments**

621 We thank Mirko Riboni, Simone Minardi, Valentina Dall'Olio, and Laura Tizzoni at Cogentech for
622 sequencing and qRT-PCR services, Dario Parazzoli and the imaging unit of IFOM, IFOM cell culture facility
623 for technical assistance

624 This work was supported by: Associazione Italiana per la Ricerca sul Cancro (AIRC IG#18621 and
625 5Xmille#22759 to GS, M.F., and C.T.; AIRC-IG-#21416 to M.F.

626 MyFirstAIRCgrant MFAG#22083 to FG; AIRC-IG #21762 and AIRC 5X1000#21091
627 to F.d.F); the Italian Ministry of University and Scientific Research (PRIN 2017, 2017HWTP2K to GS; PRIN-
628 2015SJLMB9 to M.F. and F.d.F); the European Research Council (ERC advanced grant#835103 to F.d.F);
629 Progetto AriSLA 2021 "DDR & ALS; FRRB - Fondazione Regionale per la Ricerca Biomedica - under the
630 frame of EJP RD, the European Joint Programme on Rare Diseases with funding from the European
631 Union's Horizon 2020 research and innovation program under the EJP RD COFUND-EJP N° 825575. to
632 F.g.F; from LABEX DCBIOL (ANR-10-IDEX-0001-02 PSL* and ANR-11-LABX-0043), ANR ANR-17-CE15-
633 0025-01 and ANR-18-CE92-0022-01, INSERM 19CS007-00, INCA PLBIO to N.M; INCA PLBIO 2019-1-PL
634 BIO-07-ICR-1, INSERM Plan Cancer Single Cell grant 19CS007-00 to M.P.

635
636 H.A. is supported by a fellowship from Fondazione Umberto Veronesi; L.B, from a fellowship from the
637 Associazione Italiana per la Ricerca sul Cancro.
638

639 **Author contributions:**

640 Conceptualization: GS, CT, FG, RC,

641 Methodology: EF, AP, SV, LB, HA, CM, GVB, GdC, FP, UG, VC, GN.

642 Data Analysis and quantification: FI, FZ, FG, SV, RC, WY, EM, CP, FF, CL

643 Visualization: AP, EF

644 Clinical sample acquisition, VG, GB, CT, VC, CR, ML, RC, PP, AV

645 Funding acquisition: SJE, MJM, JLS, EH

646 Supervision: MF, MP, FdF, MP, AM, VG, GB, FF, CL

647 Writing – original draft: GS, AP

648 Writing – review & editing: GS, FG, RC, CT

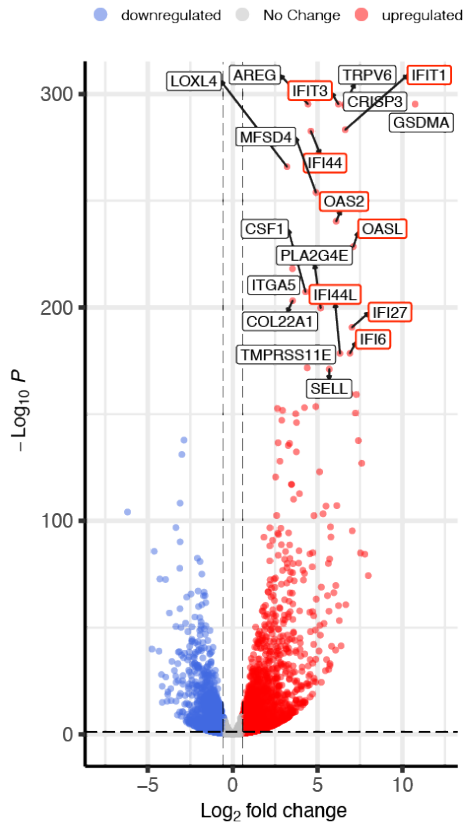
649
650 **Competing interests:** M.P. is co-founder, member of the board of directors, and stakeholder of the
651 company CheckmAb s.r.l. The remaining authors declare no competing interests.
652

653 **Data and materials availability:** RNA-seq data of MCF10A and MCF10.DCIS.com cells and organoids
654 are being submitted respectively to Gene Expression Omnibus (GEO) and European Genome-phenome
655 Archive (EGA) and are available upon request.

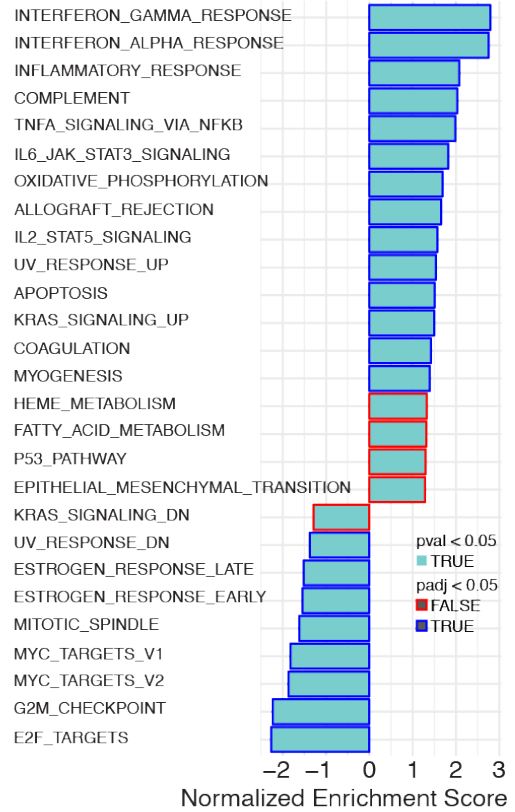
656 All other data are available in the main text or supplementary materials.

Figure 1

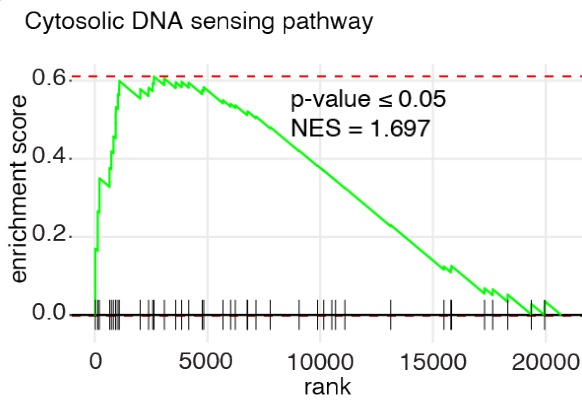
A



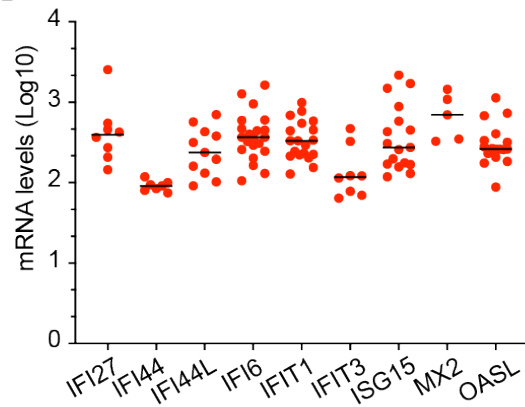
B



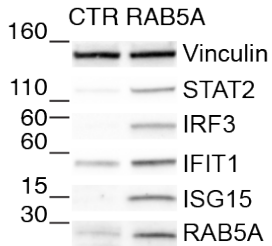
C



D



E



657
658
659

660 **Figure 1. Tissue fluidification induces a CytoDR gene signature**

661 **A.** Volcano plot representing differentially expressed genes between control empty vector and RAB5A-
662 expressing MCF10.DCIS monolayers. All significantly RAB5A-expressing deregulated genes are indicated
663 in red (upregulated) and blue (downregulated). The enrichment (\log_2 Fold Change) is plotted on the x-axis
664 and the significance (Wald test $-\log_{10}$ p-value) is plotted on the y-axis. Labels are the most upregulated
665 genes. Outlined in red are interferon-stimulated genes.

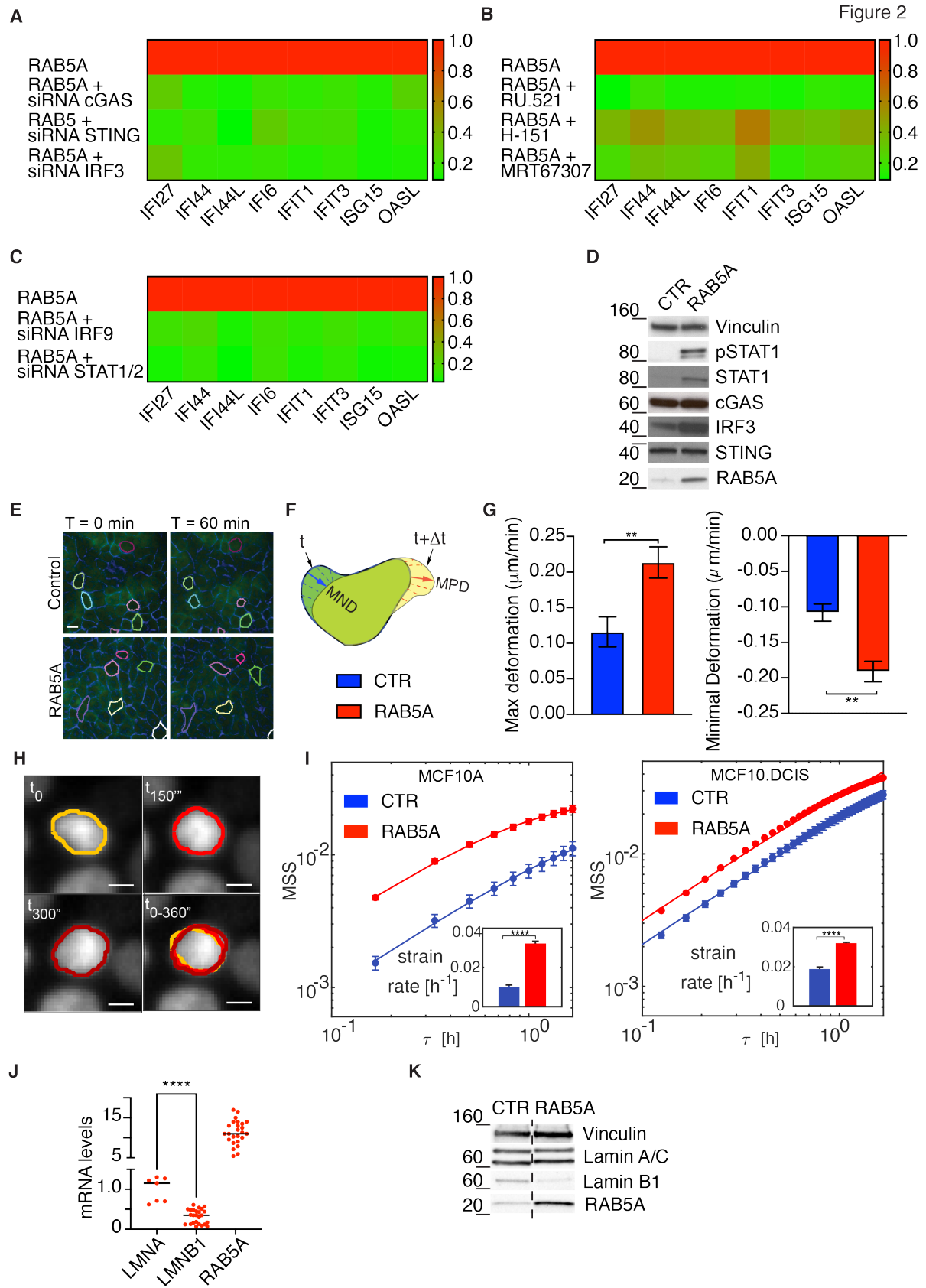
666 **B.** Gene set enrichment analysis (GSEA) of differentially expressed genes in RAB5A-expressing
667 MCF10.DCIS.com monolayer over control cells. GSEA was performed using the Hallmarks pathway gene
668 sets in the GSEA Molecular Signatures Database. Moderated t-statistic was used to rank the genes.
669 Reported are significantly enriched pathways (P-value < 0.05) with the color of the outline of the bar
670 corresponding to the BH-adjusted P-value. P-value was calculated as the number of random genes with
671 the same or more extreme ES value divided by the total number of generated gene sets.

672 **C.** GSEA Enrichment plot of differentially expressed genes in RAB5A-expressing MCF10.DCIS.com
673 monolayer using the KEGG cytosolic DNA sensing pathway (hsa04623). The green curve corresponds to
674 the ES (enrichment score) curve, which is the running sum of the weighted enrichment score obtained from
675 GSEA software, while the normalized enrichment score (NES) and the corresponding P-value are reported
676 within the graph.

677 **D.** Scatter plots of mRNA expression levels of IFI27, IFI44, IFI44L, IFI6, IFIT1, IFIT3, ISG15, MX2, and
678 OASL determined by qRT-PCR in RAB5A-expressing MCF10.DCIS monolayers relative to control cells.
679 Data are expressed as \log_{10} values, horizontal lines represent group medians. Each dot represents an
680 independent experiment. Values were normalized to the controls of each experiment

681 **E.** Immunoblots of lysates from doxycycline-treated control (CTR) and RAB5A-expressing (RAB5A)
682 MCF10.DCIS.com monolayers with the indicated antibodies. Mw is indicated on the left.

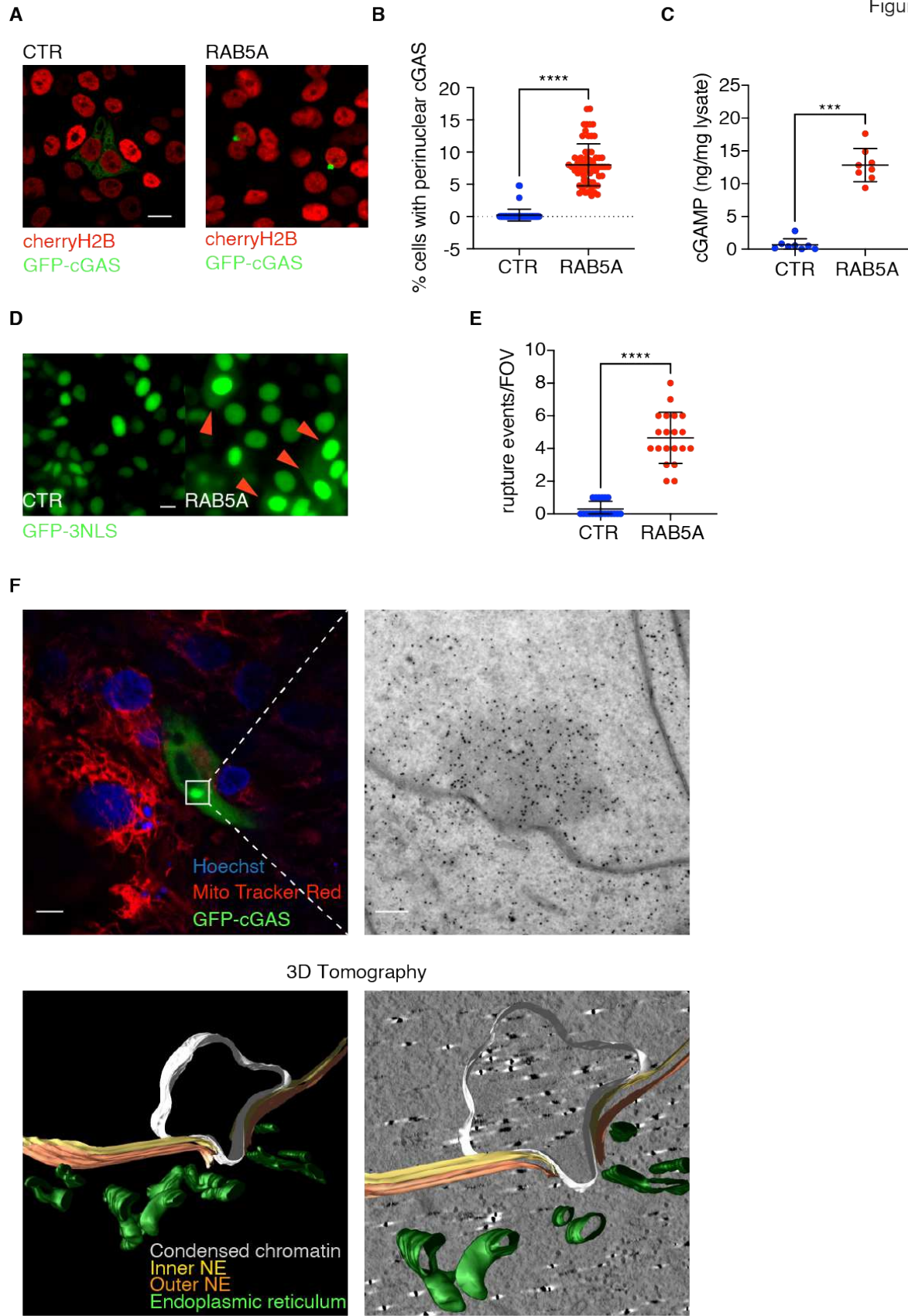
683



684
685
686

687 **Figure 2. A cGAS/STING pathway mediates tissue fluidification-dependent CytoDR genes**
688 **A.** Heatmap representing color-coded expression levels of differentially expressed CytoDR genes in
689 RAB5A-expressing MCF10.DCIS.com monolayers silenced for the indicated genes. The effectiveness of
690 silencing was determined by qRT-PCR (see also Figure S4A). The data are the ratio between the level of
691 gene expression in each of the conditions tested relative to those of mock-treated (using scramble oligos)
692 RAB5A-expressing cells. The mean \pm s.d. (at least $n = 3$ independent experiments) and P values, each-pair
693 Student's t-test (treated versus mock-treated RAB5A-expressing cells) are reported in **Table S1_Figure 2A**.
694 **B.** Heatmap representing color-coded expression levels of differentially expressed CytoDR genes in
695 RAB5A-expressing MCF10.DCIS.com monolayers treated with the indicated small molecules: cGAS
696 inhibitor, RU.521, the STING antagonist, H-151, or the TBK1/IKK inhibitor, MRT67307. The data are the
697 ratio between the level of gene expression in each of the conditions tested relative to vehicle-treated
698 RAB5A-expressing cells. The mean \pm s.d. (at least $n = 3$ independent experiments) and P values, each-pair
699 Student's t-test (treated versus untreated RAB5A-expressing cells), are reported in **Table S2_Figure 2B**.
700 **C.** Heatmap representing color-coded expression levels of differentially expressed CytoDR genes in
701 RAB5A-expressing MCF10.DCIS.com monolayers silenced for the indicated genes. The effectiveness of
702 silencing was determined by qRT-PCR. The data are the ratio between the level of gene expression in each
703 of the conditions tested relative to those of mock-treated (using scramble oligos) RAB5A-expressing cells.
704 The mean \pm s.d. (at least $n = 7$ independent experiments) and P values, each-pair Student's t-test (siRNA
705 versus RAB5A-expressing cells) are reported in **Table S3_Figure 2C**.
706 **D.** Immunoblots of lysates from doxycycline-treated control (CTR) and RAB5A-expressing (RAB5A)
707 MCF10.DCIS.com monolayers with the indicated antibodies. Mw is indicated on the left.
708 **E-G.** Area fluctuations induced by RAB5A. EGFP-CDH1, control (CTR) and RAB5A-expressing (RAB5A)
709 MCF10A monolayers seeded at a jamming density, were treated with doxycycline for 16 h and monitored
710 by time-lapse over 24 h (5 min frame-rate) (**Movie S3**). Automated image segmentation was applied to
711 identify the cell contour and area exploiting the EGFP-CDH1 fluorescence as described in methods. (**E.**)
712 Still images depicting representative examples of selected cells with their contour indicated by pseudo-
713 coloring and used for the analysis are shown at $t=0$ and $t=60$ min. Scale Bar is 10 μm . (**F.**) Scheme depicting
714 how the maximum positive deformation (MPD) and maximum negative deformation (MND) were scored
715 and computed for each cell analyzed. (**G.**) Data are the mean of maximal and minimal area deformation
716 over time. ($n=80$ cells/conditions in one representative experiment out of four). ** $p < 0.005$, Mann-Whitney
717 paired-t-test
718 **H.** Nuclear segmentation. Representative consecutive frames centered on the same RAB5A-expressing
719 MCF10A nucleus. Continuous lines with different shades of red represent the corresponding profiles
720 obtained *via* nuclear segmentations. In the bottom right panel, the superposition of the three profiles is also
721 shown, illustrating the characteristic shape variations the nucleus undergoes. Scale bar, 5 μm
722 **I.** Comparison of the nuclear mean square strain (MSS) of control and RAB5A-expressing cells in MCF10A
723 (left panel) and MCF10.DCIS.com (right panel) monolayers. In each condition, the MSS is obtained by
724 tracking and segmenting N nuclei over the time window 4-20 h ($N>5000$ and $N>1000$ for control and
725 RAB5A-expressing MCF10A monolayers, respectively; $N>700$ and $N>400$ for control and RAB5A-
726 expressing MCF10.DCIS.com monolayers, respectively). Continuous lines are best fitting curves to the data
727 with an exponential model. The initial slope of each curve enables estimating the corresponding nuclear
728 strain rate, which is reported in the inset of each panel as mean \pm s.d. ($n= 10$ randomly populated subsets
729 of cells). **** $p < 0.0001$, P values, T-test (CTR versus RAB5A).
730 **J.** Scatter plot of the mRNA expression levels of LMNA, LMNB1, and RAB5A determined by qRT-PCR in
731 RAB5A-expressing MCF10.DCIS.com over control monolayers. The data are the mean (at least $n = 7$
732 independent experiments). **** $p < 0.0001$, P values, each-pair Mann Whitney test (LMNA versus LMNB1).
733 **K.** Immunoblots of doxycycline-treated control (CTR) and RAB5A-expressing (RAB5A) MCF10.DCIS.com
734 monolayers with the indicated antibodies. Mw is indicated on the left.
735
736
737
738
739
740
741
742
743

Figure 3



746
747
748
749
750
751
752
753
754
755
756
757
758
759
760
761
762
763
764
765
766
767
768
769
770
771

Figure 3. Nuclear envelope ruptures activate cGAS in fluidized monolayers

A. Immunofluorescence images of doxycycline-treated control (CTR) and RAB5A-expressing (RAB5A) mcherry-H2B MCF10.DCIS.com monolayers transfected with EGFP-cGAS. Scale bar 20 μm .

B. Scatter plot of the percentage of MCF10.DCIS.com cells with perinuclear cGAS enrichment is expressed as the mean \pm s.d. (at least $n=10$ FOV/experimental conditions in 3 independent experiments). **** $p < 0.0001$, P values, each-pair Mann Whitney test (CTR versus RAB5A).

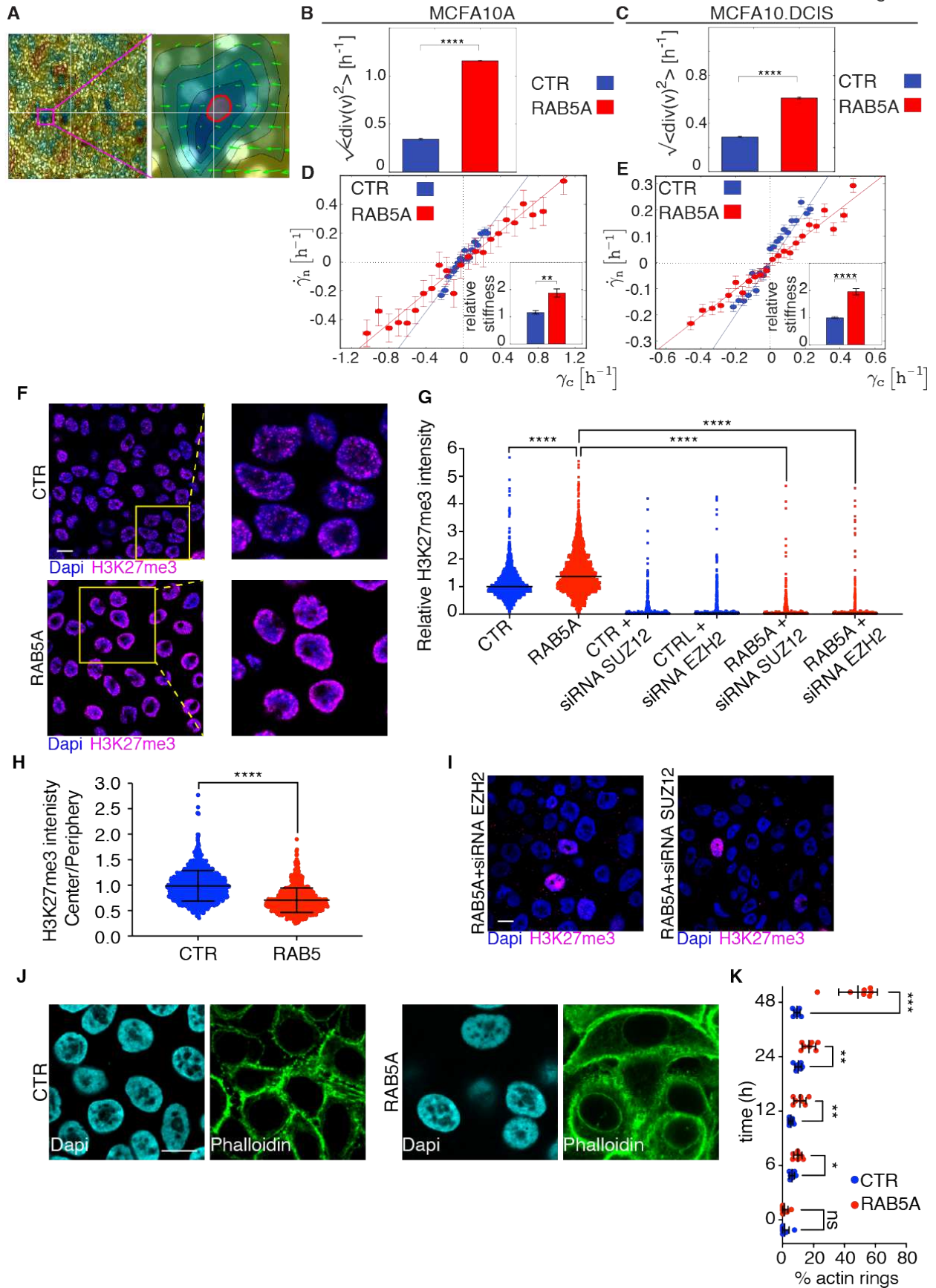
C. Scatter plot of the quantification of cGAMP by ELISA from control (CTR) and RAB5A-expressing (RAB5A) MCF10.DCIS.com cell extracts. Data are the cGAMP amounts (ng) per mg of total cell extract expressed as the mean \pm s.d. (at least $n=3$ independent experiments). **** $p < 0.0001$, P values, each-pair Welch's test (CTR versus RAB5A).

D. Snapshot of time-lapse ([Movie S6](#)) EGFP-3NLS-expressing control (CTR) and RAB5A-MCF10.DCIS.com monolayers displaying events of NE rupture and EGFP-3NLS leakage (red arrowheads). Scale bar 10 μm .

E. Scatter plot of the number of nuclear envelope rupture events/FOV reported as mean \pm s.d. ($n=10$ FOV/experimental conditions in 2 independent experiments). **** $p < 0.0001$, P values, each-pair Mann Whitney test (CTR versus RAB5A).

F. CLEM analysis of cGAS perinuclear foci. RAB5A-expressing MCF10.DCIS.com cells monolayers transfected with EGFP-cGAS were plated on MaTek dishes with grid and stained with Hoechst and Mito Tracker Red to detect nuclei and mitochondria respectively (upper left). Scale bar 5 μm . Cells identified on grids by confocal microscopy were processed for electron microscopy and z-axis serial sections were stained with gold-labeled anti-GFP antibody to detect EGFP-cGAS (upper right). Scale bar 500 nm. Images of three-dimensional tomographic reconstruction and 3D model of a nuclear envelope rupture site (bottom panels).

Figure 4



774 **Figure 4. Tissue fluidification induces nuclear stiffness, heterochromatin reorganization, and actin**
775 **remodeling**

776 **A.** Left panel: representative map of the divergence of the velocity field in MCF10A RAB5A-expressing
777 monolayer. The velocity field is obtained from PIV. Cold (warm) colors correspond to negative (positive)
778 values of the divergence. Right panel: enlarged view of a small portion (70x70 μm) of the map shown on
779 the left, centered on a selected nucleus (outlined in red). In this case, the velocity field (green arrows) points
780 mainly towards the central cell. Locally, this corresponds to a negative value of the divergence and thus to
781 a compressive deformation of the cell, which we systematically compare with the simultaneous nuclear
782 deformation.

783 **B-C.** Root mean square value of the divergence of the velocity field obtained from PIV over the time window
784 4-20 h for MCF10A (**B**) and MCF10.DCIS.com (**C**) monolayers. Results are the mean \pm s.d.. [5 different
785 FOVs (corresponding to roughly $1.2 \cdot 10^4$ cells)/ condition and 4 different FOVs (corresponding to roughly
786 $8 \cdot 10^3$ cells)/ condition for MCF10A and MCF10.DCIS.com monolayers, respectively].
787 **** $p < 0.001$, P values, t-test (CTR versus RAB5A).

788 **D-E.** Nuclear strain rate $\dot{\gamma}_n$ as a function of the corresponding cell strain rate $\dot{\gamma}_c$ for MCF10A (**D**) and
789 MCF10.DCIS.com (**E**) monolayers. $\dot{\gamma}_n$ is obtained from nuclear segmentation, while $\dot{\gamma}_c$ is estimated from
790 the divergence of the velocity field measured with PIV. For clarity, data are grouped into evenly spaced bins
791 along the horizontal axis. Symbols and error bars are the mean value and standard deviation of the $\dot{\gamma}_n$ -
792 values of the data included in each bin, respectively. Straight lines are best fitting curves to the data with a
793 linear model $\dot{\gamma}_n = s \dot{\gamma}_c$. Insets: relative nuclear stiffness, estimated as the inverse $1/s$ of the slope obtained
794 from the corresponding fitting model which is reported as mean \pm s.d. ($n=10$ randomly populated subsets
795 of cells). ** $p < 0.01$, **** $p < 0.0001$, P values, T-test (CTR versus RAB5A).

796 **F.** Immunofluorescence images of doxycycline-treated control (CTR) and RAB5A-expressing (RAB5A)
797 MCF10.DCIS.com monolayers stained with Dapi and anti-H3K27me3 antibody to detect nuclei and
798 heterochromatin, respectively. Magnified images from the selected yellow boxes are shown. Scale bar 10
799 μm .

800 **G.** Scatter plot of relative H3K27me3 intensity of control (CTR) and RAB5A-expressing (RAB5A)
801 MCF10.DCIS.com monolayers silenced or not for EZH2 or SUZ12. Each dot represents a cell and the
802 median is indicated. ($n > 1400$ cells/experimental condition for CTR and RAB5A, $n > 400$ cells/experimental
803 condition for siRNA-treated conditions). **** $p < 0.0001$, P values, Kruskal-Wallis/Dunn's test.

804 **H.** Scatter plot of the ratio of H3K27me3 intensity at the nuclear central region over the nuclear periphery
805 of control (CTR) and RAB5A-expressing (RAB5A) MCF10.DCIS.com. Each dot represents a cell and the
806 mean \pm s.d. is indicated. ($n > 1000$ cells/experimental condition pooled from 3 independent experiments).
807 **** $p < 0.0001$, P values, Mann-Whitney test.

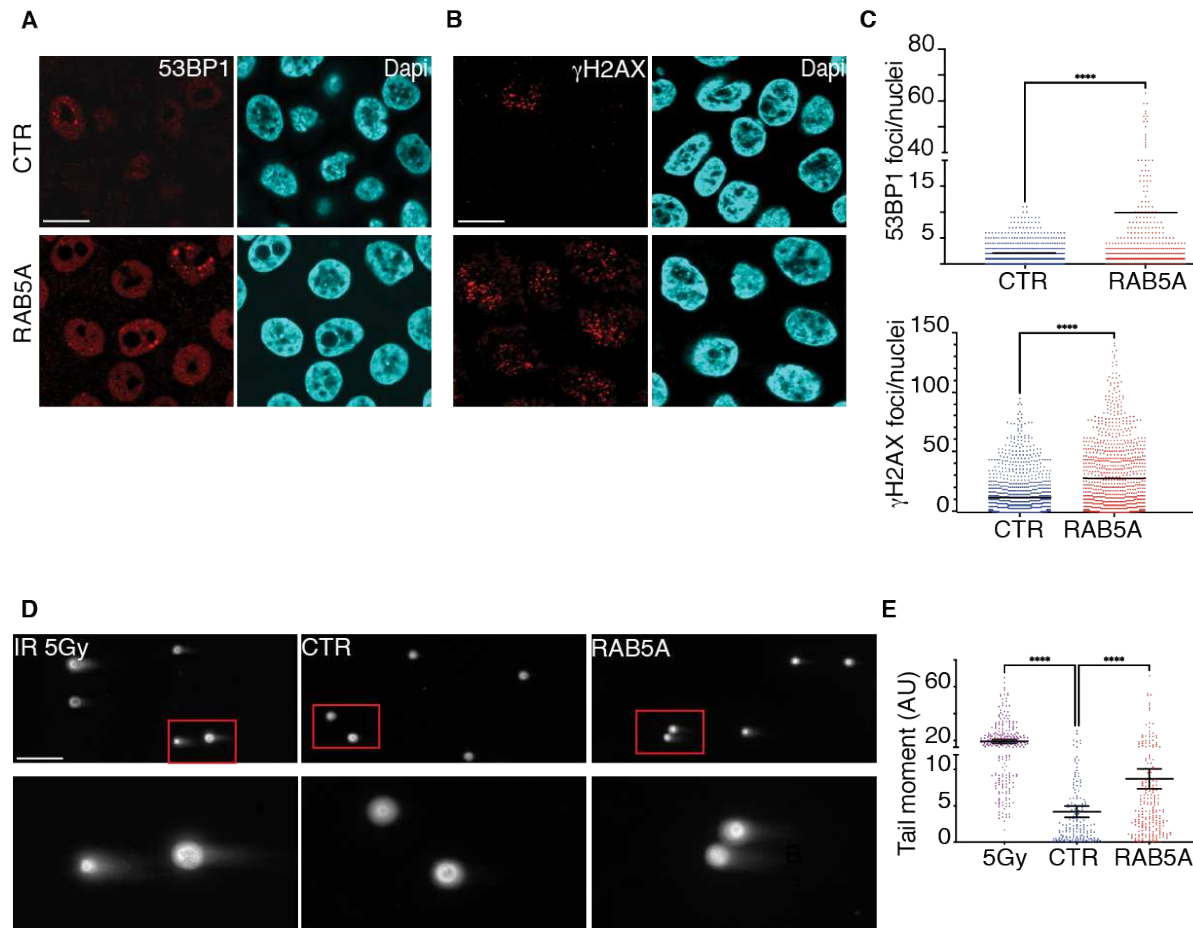
808 **I.** Immunofluorescence images of control empty vector (CTR) and RAB5A-expressing (RAB5A)
809 MCF10.DCIS.com monolayers silenced for EZH2 or SUZ12 and stained with DAPI and anti-H3K27me3
810 antibody to detect nuclei and heterochromatin, respectively. Scale bar 10 μm .

811 **J.** Immunofluorescence images of control (CTR) and RAB5A-expressing (RAB5A) MCF10.DCIS.com
812 monolayers stimulated with doxycycline to induce RAB5A expression, fixed at various time points and
813 stained with phalloidin to detect F-actin. Representative images of duplicate experiments are a
814 magnification of 48 h time points to show actin ring structures. Scale bar 20 μm .

815 **K.** Scatter plot of the percentage of actin ring structures/FOV at the indicated time points. Data are
816 expressed as the mean \pm s.d. ($n = 2$ independent experiments). ns > 0.999 , * $p < 0.05$, ** $p < 0.01$, *** $p <$
817 0.001 , P values, each-pair Mann Whitney test (CTR versus RAB5A).

818

Figure 5



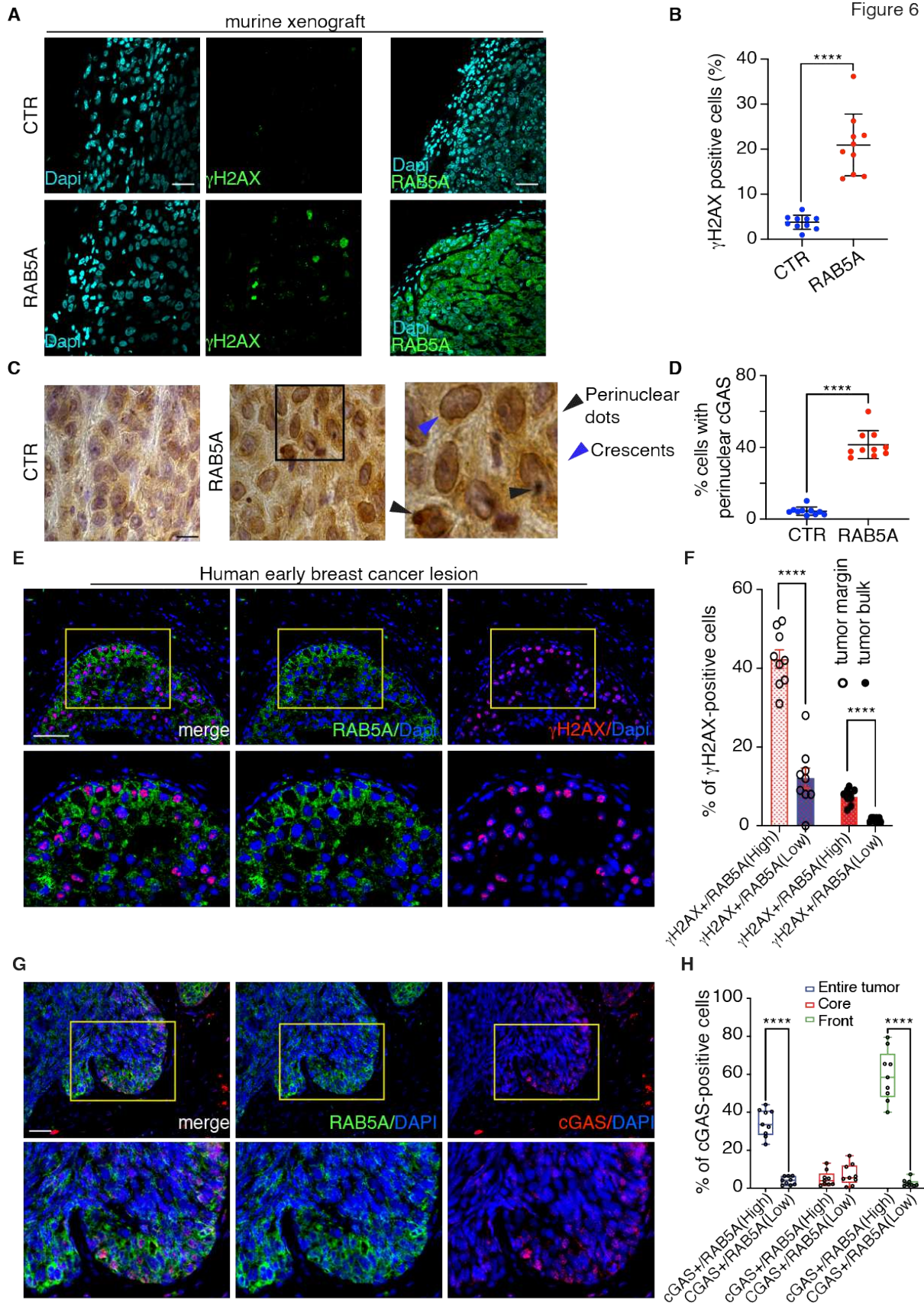
819
820
821 **Figure 5. Endocytic-dependent tissue fluidification results in DNA damage**

822 **A-B.** Images of control and RAB5A-MCF10.DCIS.com monolayers stained with the indicated antibodies.
823 Scale bar, 20 μ m.

824 **C.** The scatter plot shows the mean of 53BP1 foci/nuclei or γ H2AX foci/nuclei
825 ($n > 150$ out of three independent experiments). **** $p < 0.001$, P values, unpaired Mann Whitney t-test
826 (CTR versus RAB5A).

827 **D.** Representative images of neutral comet assay carried out in MCF10.DCIS.com monolayer cells
828 expressing RAB5A. Control cells irradiated (IR 5Gy) or not (CTR) are also shown. Scale bar, 100 μ m.

829 **E.** The scatter plot shows the quantification of DNA damage by tail moment analysis. Horizontal bars
830 indicate the means and s.d. of at least 2 independent experiments; more than 100 cells per sample were
831 scored. **** $p < 0.001$, P values, one-way ANOVA.



834
835
836
837
838
839
840
841
842
843
844
845
846
847
848
849
850
851
852
853
854
855
856
857
858
859
860
861
862
863
864
865
866
867
868
869
870
871
872

Figure 6. Increased RAB5A-expression, cGAS perinuclear accumulation, and DNA damage in human invasive ductal carcinoma

A. Immunofluorescence images of control (CTR) and RAB5A-expressing (RAB5A) MCF10.DCIS.com injected into mammary fat pads of immunocompromised mice. After one week, mice were fed with doxycycline to induce RAB5A expression. Four weeks after doxycycline treatment, primary tumors were isolated, fixed and stained with Dapi and γ H2AX to detect nuclei and DNA damage foci, respectively. The samples were also stained with Dapi and RAB5A. Scale bar 100 μ m.

B. Scatter plot of the percentage of γ H2AX positive cells/FOV. Data are mean \pm s.d. ($n=2$ independent experiments, with 5 mice/experiment). **** $p < 0.0001$, P values, each-pair Welch's test (CTR versus RAB5A).

C. Immunohistochemical analysis of cGAS expression and localization in control (CTR) and RAB5A-expressing (RAB5A) MCF10.DCIS.com injected into mammary fat pads of immunocompromised mice. After one week, mice were fed with doxycycline to induce RAB5A expression. Four weeks after doxycycline treatment, primary tumors were isolated, fixed and stained with a specific cGAS antibody. The right panel shows a higher magnification of the boxed region to display enhanced levels of cGAS with perinuclear dotted (black harrow-heads) or crescent-like distribution (blue harrow-head). Scale bar 80 μ m.

D. Scatter plot of the percentage of cells with perinuclear cGAS enrichment is expressed as the mean \pm s.d. (at least $n = 5$ FOV/experimental conditions in two independent experiments). **** $p < 0.0001$, P values, each-pair Mann Whitney test (CTR versus RAB5A).

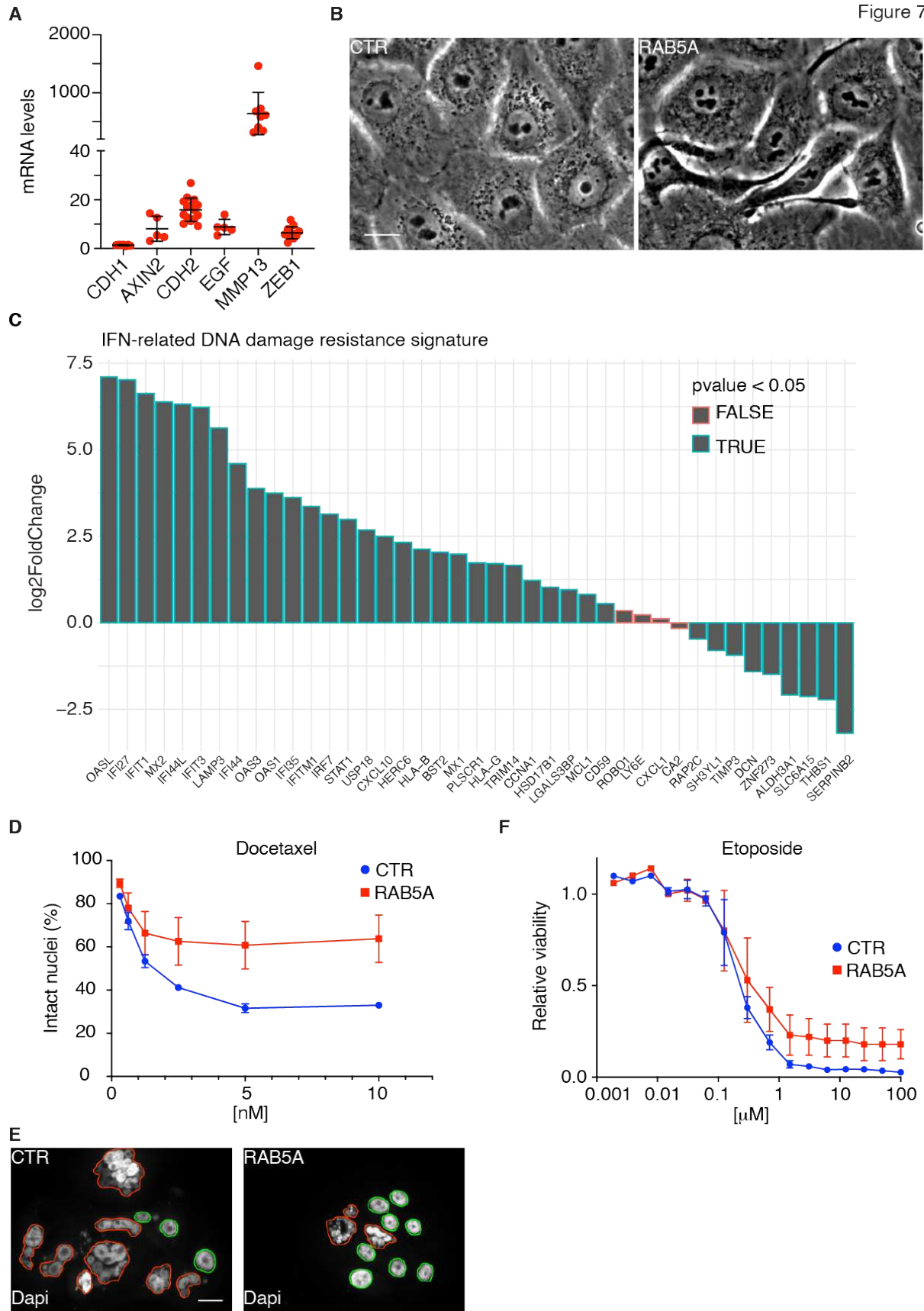
E. Representative multiplex immunohistochemistry/Immunofluorescence (mIHC/IF) of RAB5A, γ H2AX and Dapi in human Ductal breast Carcinoma *in Situ* (DCIS). Magnified images from the selected yellow boxes are shown. Scale bar 150 μ m.

F. Box and scatter plots showing the percentage of γ H2AX -positive nuclei in cells that express high (>2 on a scale from 0.1,2,3) or low (< 2 on a scale from 0.1,2,3) levels of RAB5A in the tumor bulk or margin (defined by an automated, operator-independent analysis of all cell nuclei at a set distance from the tumor edge versus those nuclei present in the tumor bulk-see methods for details and [Movie S9](#)). The areas of 9 independent DCIS were analyzed with more than 200 nuclei per area. **** $P < 0.0001$, Nested 1 way ANOVA test.

G. Representative multiplex immunohistochemistry/immunofluorescence (mIHC/IF) of RAB5A, cGAS, and Dapi in human Ductal breast Carcinoma *in Situ* (DCIS). Magnified images from the selected yellow boxes are shown. Scale bar 300 μ m.

H. Box and scatter plots showing the percentage of cGAS-positive cells that express high (>2 on a scale from 0.1,2,3) or low (< 2 on a scale from 0.1,2,3) levels of RAB5A in the tumor bulk, or the margin or the whole tumor (the margin and tumor bulk were defined by an automated, operator-independent analysis of all cell nuclei at a set distance from the tumor edge versus those nuclei present in the tumor bulk-see methods for details). The areas of 9 independent DCIS were analyzed with more than 200 nuclei per area. **** $P < 0.0001$, Mann-Whitney two-tailed t-test.

Figure 7



875 **Figure 7. Tissue fluidification enhances plastic EMT traits and chemoresistance**
876 **A.** Scatter pots of the mRNA expression levels of CDH1, AXIN2, CDH2, EGF, MMP13, and ZEB1
877 determined by qRT-PCR in RAB5A-expressing MCF10.DCIS.com monolayers over control cells. Data are
878 the mean \pm s.d. (at least n = 5 independent experiments). Values were normalized to the controls of each
879 experiment.
880 **B.** Phase-contrast images of control empty vector (CTR) and RAB5A-expressing (RAB5A)
881 MCF10.DCIS.com monolayer. Scale bar, 20 μ m.
882 **C.** Quantitative changes in the expression of the INF-related DNA damage resistance signature genes in
883 RAB5A-expressing MCF10.DCIS monolayers with respect to their respective controls. The log2Fold
884 Change is plotted on the x-axis and the significance (Wald test p-value) is defined by the color code of the
885 outline.
886 **D.** Percentage of intact nuclei after treatment with the indicated doses of docetaxel in control (CTR) and
887 RAB5A-expressing (RAB5A) MCF10.DCIS.com cells. Data are the mean \pm s.d. (n=3 independent
888 experiments).
889 **E.** Representative images of control empty vector (CTR) and RAB5A-expressing (RAB5A)
890 MCF10.DCIS.com nuclei stained with Dapi in the presence of 10nM Docetaxel. Intact and aberrant
891 polynucleated cell nuclei are indicated by green and red contours. Scale bar 10 μ m.
892 **F.** Dose-dependent analysis of cell proliferation of control (CTR) and RAB5A-expressing (RAB5A)
893 MCF10.DCIS.com treated with the indicated concentrations of Etoposide. Data are the mean \pm s.d. (n=3
894 independent experiments).
895

Supplementary Files

This is a list of supplementary files associated with this preprint. Click to download.

- [MovieS5.mp4](#)
- [MovieS8.mp4](#)
- [MovieS4.mp4](#)
- [MovieS7.mp4](#)
- [MovieS6.mp4](#)
- [MovieS1.mp4](#)
- [MovieS3.mp4](#)
- [MovieS9.mp4](#)
- [MovieS2.mp4](#)
- [supplementaryinformation.pdf](#)